Erosional impact on fault segmentation in thrust belts: Low-temperature thermochronology and fluvial shear stress analyses on an aftershock gap along eastern margin of Tibetan Plateau

Yijia Ye[1], Xibin Tan[1,*], Yiduo Liu[2], Feng Shi[1], Yuan-Hsi Lee[3], Jiangfei Hou[1], and Li Qian[1]

1 State Key Laboratory of Earthquake Dynamics, Institute of Geology, China Earthquake Administration, Beijing, 100029, China

2 Department of Earth and Atmospheric Sciences, University of Houston, Houston, TX, 77204-5007, USA

3 Department of Earth and Environmental Sciences, National Chung-Cheng University, Chia-Yi, 62102, Taiwan

Abstract

Mechanism for fault segmentation in thrust belt is a key to understanding the orogenic process and seismic risks. A ~50 km long aftershock gap emerged between the ruptures of the 2008 Wenchuan and the 2013 Lushan earthquakes along the eastern margin of the Tibetan Plateau. Previous studies suggested that weak materials under ductile deformation cause the gap. Here we propose an alternative explanation: differential erosion drives the along-strike variation in fault activity. To testify the two competing models, we conducted low-temperature thermochronology and fluvial shear stress analyses to depict the spatial distributions of erosion. We obtained eight apatite fission track dates (6-44 Ma) in the gap and deduced erosion rates of 0.5-0.6 mm/yr and 0.3-0.4 mm/yr since ~8 Ma in the hanging -wall and footwall of the Shuangshi-Dachuan fault, respectively. We carried out linear fitting based on an empirical relationship between thermochronology-derived erosion rate and fluvial shear stress, and then calculated the erosion rate for each survey point of fluvial shear stress. Our new data reveal that in the hinterland, the erosion rate at the gap is lower than that of adjacent areas along strike, whereas in the range front, the erosion rate at the gap is greater. This spatial pattern supports the “differential erosion” hypothesis and is at odds with the “weak material” model. This study illustrates that heterogeneous erosion regulates fault segmentation in this thrust belt. Moreover, the aftershock gap acts as a barrier for the past major earthquakes, which poses substantial seismic potential to this region.

Key Points

1. Erosion rates (0.5-0.6 and 0.3-0.4 mm/yr across the Shuangshi-Dachuan fault) in aftershock gap of Longmen Shan.
2. Spatial pattern of erosion along and across Longmen Shan supports heterogeneous erosion model.
3. Differential erosion regulates fault segmentation and points to barrier model for Longmen Shan seismicity.

1. Introduction

Thrust belt is ubiquitously characterized by segmentation. Most of the fault segmentation results from geometrical and/or lithological changes along fault strike (e.g., Mazzoli et al., 2005; Jin et al., 2010; C. Sun et al., 2019). Some, however, are controlled by erosion (e.g., Norris and Copper, 1997; Horton, 1999), a mechanism that is arguably underappreciated. This study introduces a new example of thrust segmentation under erosional control and a method to distinguish such a mechanism.

The Longmen Shan range, located along the eastern margin of the Tibetan Plateau, possesses steep relief and active tectonics (S.F. Chen et al., 1994; Clark and Royden, 2000; Kirby et al., 2002; Yin et al., 2010). The 2008 M_w 7.9 Wenchuan and 2013 M_w 6.6 Lushan earthquakes are the most catastrophic events in recent decades, causing huge casualties and property losses (**Fig. 1**) (Xu et al., 2009; Shen et al., 2009; Xu et al., 2013). A segment ~50 km long between the ruptures of the 2008 Wenchuan earthquake and the 2013 Lushan earthquake has remained unruptured in both events, and is called an ‘‘aftershock gap” (Pei et al., 2014). To understand the nature of the gap, previous studies focused on the velocity structure of the lithosphere (Z.W. Li et al., 2013; Pei et al., 2014; Liang et al., 2018) and paleo-earthquake records on the major faults (H. Wang et al., 2015; Dong et al., 2017; Shao et al., 2019). Several seismological studies found low-velocity anomalies in the upper crust within the gap, and suggested weak materials that accommodate ductile deformation and inhibit large earthquakes (Z.W. Li et al., 2013; Pei et al., 2014; Z. Liu et al., 2018). However, low-velocity anomalies are not restricted in this gap; other regions with similar

low-velocity zones do not exhibit a seismic or aftershock gap (e.g., Z. Liu et al., 2018). Moreover, as detailed in Discussion, the "weak material" model would predict morphotectonic features that are inconsistent with the surface geology (**Fig. 1**). Here we propose an alternative hypothesis: differential erosion induced along-strike variations in fault activity, which inhibited the seismic rupture propagation during the Wenchuan and Lushan earthquakes in the gap.

While both models can lead to an aftershock gap, their predictions on the spatial distributions of deformation and denudation differ. In the context of the critical-taper wedge theory (Davis et al., 1983; Suppe, 2007), which is applicable to the Longmen Shan thrust belt (Hubbard et al., 2010), the first model would result in more intense deformation in the hinterland and weaker deformation at the range front at the aftershock gap than surrounding regions along strike, whereas the second model predicts the opposite scenario (Y. Liu et al., in review). Denudation pattern is a good proxy to characterizing the deformation patter (e.g., Tian et al., 2013; Tan et al., 2019), and therefore a useful measure to test the competing mechanisms.

In this study, we report eight apatite fission track (AFT) dates in the aftershock gap and perform low-temperature thermochronological modeling using HeFTy (**Fig. 2a**). We further calculate the fluvial shear stress in rivers within the gap and adjacent portions, as a proxy for incision intensity to gain a wider distribution of erosion (**Fig. 2b**) (Lavé and Avouac, 2001; Godard et al., 2010). These results are compared with the predicted deformation and denudation patterns of the competing models, with an attempt to advance our understanding on the segmentation in thrust belts.

2. Geological Setting

The Longmen Shan is located along the eastern margin of the Tibetan Plateau, adjacent to the Sichuan Basin (**Fig. 1**). Within 50 km of distance across the Longmen Shan, the mean elevation ascends dramatically from ~500 m in the Sichuan Basin to over 5,000 m above sea level in the Tibetan Plateau, forming the steepest topographic gradient in the Tibetan Plateau region and, arguably, of the world (Clark & Royden, 2000; Kirby et al., 2002). Four tectonostratigraphic units exist in the Longmen Shan, including: (1) Precambrian crystalline basement of gneisses and granitoids; (2) Neoproterozoic-Permian passive margin sedimentary sequence; (3) Triassic flysch sequence in the Songpan-Ganze terrane of the Tibetan Plateau; and (4) Mesozoic-Cenozoic sedimentary rocks in the Yangtze Craton of the South China Block (Burchfiel et al., 1995; Kirby et al., 2002).

The Longmen Shan is a reactivated orogen (Jia et al., 2006; M. Sun et al., 2018; Tan et al., 2019). It was an intra-continental fold-and-thrust belt during the Mesozoic, accommodating transpressional convergence between the Songpan-Ganze terrane and the Yangtze Craton (Burchfiel et al., 1995; de Sigoyer et al., 2014). In the Cenozoic, following the Indian-Eurasian collision (Royden et al., 1997; Yin and Harrison, 2000; Tapponnier et al., 2001), the outward growth of the Tibetan Plateau reactivated many faults along the eastern Tibetan Plateau margin; collectively, they form the Longmen Shan thrust belt (**Fig. 1**).

The northeast-trending Longmen Shan thrust belt (500 km long and 30-60 km wide) consists of several sub-parallel, NW-dipping thrust faults. From northwest to southeast in the central segment, the faults are Wenchuan-Maoxian (WMF), Beichuan-Yingxiu (BYF), and Jiangyou-Guanxian fault, respectively. Sub-parallel major thrust faults are also present in the southern Longmen Shan, including the Wulong-Yanjing fault (WYF) and the Shuangshi-Dachuan fault (SDF) (**Fig. 1**). These faults are top-to-the-east, imbricated thrusts with a generally foreland-ward propagation history in the Late-Cenozoic based on seismic- and field-based structural analyses and low-temperature thermochronology (Hubbard & Shaw, 2009; Lu et al., 2014; Tan et al., 2017). Crustal deformation has propagated into the Sichuan Basin, culminating in the development of the Dayi fault, Xiongpo fault, Longquan Shan fault, and associated fault-related folds (Jia et al., 2006; C. Sun et al., 2016). GPS measurements show horizontal shortening rates are less than 3 mm/year across the Longmen Shan thrust belt (Gan et al., 2007; G. Zheng et al., 2017).

Five major earthquakes took place during the past 1000 years (**Fig. 1**). The 1327 *M* 6 and 1941 *M* 6.2 Tianquan earthquake occurred near the southern end of the Longmen Shan. The 1970 M_s 6.2 Dayi earthquake occurred in the current aftershock gap. The 12 May, 2008 M_w 7.9 Wenchuan earthquake ruptured the surface in the central and northern segments of the Longmen Shan along the BYF and Jiangyou-Guanxian fault (e.g., Xu et al., 2009; Liu-Zeng et al., 2009). The 20 April, 2013 M_w 6.6 Lushan earthquake struck the south Longmen Shan. After the Lushan earthquake, based on detailed field investigations, no surface rupture has been found;

only local compression ruptures were observed in concrete roads along the SDF (Xu et al., 2013). According to the aftershock relocation, the 2008 Wenchuan earthquake and the 2013 Lushan earthquake has a rupture length of ~300-350 km and ~35 km, respectively (Huang et al., 2008; Y. Zheng et al., 2009; Fang et al., 2013, 2015). A gap of ~50 km long is present in-between.

3. Low-temperature Thermochronology

3.1. Previous Studies

In the central and southern Longmen Shan, previous studies reported abundant low-temperature thermochronology dates, as compiled in **Fig. 2a**. Arne et al. (1997) and Kirby et al. (2002) reported the first low-temperature thermochronology evidence of Late-Cenozoic rapid exhumation, with the method of fission track and (U-Th)/He, respectively. Xu et al. (2000) and Wilson et al. (2011) reported fission track dates to reveal Cenozoic incision histories in the plateau interior. Godard et al. (2009) showed that the samples of Pengguan massif began to rapidly denudate at a rate of ~0.65 mm/yr since ~10 Ma according to (U-Th)/He dating and modeling. E. Wang et al. (2012) systematically studied the low-temperature thermochronology of profile samples in the Pengguan massif with elevation difference of ~3000 meters. They obtained the Cenozoic cooling history of the Pengguan massif and discovered two periods of rapid cooling events (30-25 Ma and 10-0 Ma). Tan et al. (2017) and Shen et al. (2019) sampled the Xuelongbao massif in the hanging-wall of WMF, and unveiled

153 a rapid phase of denudation since 11-14 Ma with a rate of 0.8-1.2 mm/yr. Several
154 groups took detailed study in the Qingyi Jiang basin at the southern Longmen Shan,
155 and documented a rapid denudation history of rock masses on both sides of the
156 Wulong-Yanjing fault (WYF) since the Late Miocene (Tian et al., 2013; Cook et al.,
157 2013; Tan et al., 2014). Coincidentally or not, previous studies have mainly focused
158 on the Min Jiang and Qingyi Jiang drainage basins, largely overlapping the zones of
159 the 2008 Wenchuan and 2013 Lushan earthquake sequences, respectively.
160 Low-temperature thermochronology data is lacking within the aftershock gap,
161 inhibiting a systematic comparison of exhumation history along strike (**Fig. 2a**).
162

163 ## 3.2. Sampling Strategy, Method, and Results

164 In order to constrain the Late-Cenozoic exhumation and faulting activities in the
165 aftershock gap of the Longmen Shan, we collected samples passing through the major
166 faults. To minimize the influence of elevation, all samples were collected in valley
167 bottoms. Because of the widespread limestone and mudstone in the study area, only
168 eight samples yielded sufficient apatite grains for AFT dating. Their locations are
169 listed in **Table 1** and plotted in **Fig. 2(a)**.
170 Sample preparation and experimental method followed T. Liu et al. (2001). Two
171 standard glass pieces, NBS SRM-612, calibrated against the fission-track age standard
172 Fish Canyon Tuff (Naeser et al., 1981), were wrapped tightly and irradiated with the
173 samples. Grain-by-grain and mica external detector techniques were adopted to obtain

individual grain ages (Wagner and Van den Haute, 2012). The Zeta value for the standard glasses SRM-612 was 348.38 ± 20.7 (1σ) (Green, 1985; Hurford and Green, 1983).

Fig. 3 and **Table 1** show the eight AFT ages and age spectra. AFT dating yield two dates of ~6 Ma between the WYF and SDF (DY-01 and 04), and six dates between ~18 and 44 Ma in the range front area between the SDF and Dayi fault (DY-06, 07, 08, 12, 13, and 14). Three of the eight samples (i.e., DY-07, 08, and 14) yield sufficient track length for thermal history modeling, as detailed below.

3.3. Modeling and Interpretations on AFT Data

Low-temperature thermochronology is a powerful approach to elucidate cooling history of rock samples. In this study, we use the AFT method with closure temperature (110±10°C) (Brandon et al., 1998; Donelick et al., 2005). One advantage of the AFT method is that the length distribution of fission tracks carries information about the thermal history from closure temperature to surface temperature (e.g., Willett, 1997; Ketcham et al. 2007), especially for relative old samples.

Samples DY-01 and DY-04 located between the WYF and SDF yield young ages of ~6 Ma. As they have very few spontaneous tracks, it is difficult to gather enough track length for thermal history modeling. However, the young ages (~6 Ma) indicate a rapid cooling rate (~15°C/Ma) from the closure temperature (110±10°C) to the ground surface temperature (~20°C) within ~6 Myr.

The other six samples located between the SDF and the Dayi fault show AFT

ages of ~20-44 Ma. Three of them (DY-07, 08, 14) resulted in sufficient (~100) fission track length measurements. We used HeFTy tool to model their thermal histories, based upon the annealing model by Ketcham et al. (2007). The modeling results are shown in **Fig. 4**. All goodness of fit (GOFs) are greater than 0.9, indicating high reliabilities (**Fig. 4**). We further utilized TERRA software (Ehlers, 2005) to convert the cooling history to denudation history. The observed cooling history of samples DY-07, 08, and 14 (all in the footwall of SDF) fit best with the denudation rates between 0.3 and 0.4 mm/yr, while the cooling history of DY-01 and 04 from the hanging-wall of SDF fit best with a denudation rate between 0.5 and 0.6 mm/yr (**Fig. 5**).

4. Fluvial shear stress

4.1. Theoretical background

Mechanical processes, including the rolling of bed load or suspended load, weathering, and cavitation, cause bedrock incision. Channel river's gradient and drainage area have a relationship with the rate of fluvial incision as a power function (Howard, 1994):

$$i = KA^m S^n \quad (1)$$

where i is incision rate, K is erodibility coefficient, A is drainage area, and S is river gradient. Three physical variables, including stream power, unit stream power, and fluvial shear stress, can lead to Eq. (1) (Howard et al., 1994; Slingerland et al., 1998).

While it is difficult to discriminate these variables' roles in incision, especially between unit stream power and fluvial shear stress (Snyder et al., 2000), experiment in the sub-Himalaya found that the fluvial shear stress correlates more consistently to river incision rate than does the unit stream power (Lavé and Avouac, 2001).

The fluvial shear stress (τ) is defined as,

$$\tau = \rho g R S \quad (2)$$

where ρ is water density, g is gravitational acceleration, R is hydraulic radius, and S is stream slope. The hydraulic radius R is a function of channel width W and water depth h (Lavé and Avouac, 2001)

$$R = \frac{Wh}{W+2h} \quad (3)$$

The water depth can be expressed as a function of water discharge Q, channel width W and depth-averaged velocity U (Manning's equation) (Chang, 1988),

$$U = \frac{Q}{Wh} = \frac{1}{N} R^{2/3} S^{1/2} \quad (4)$$

where N is roughness coefficient ($N \propto D_{90}^{1/6}$, D_{90} is the grain diameter not exceeded by 90% (in weight) of the bed load), and water discharge Q follows a power law function of the drained area (Lavé and Avouac, 2001; Godard et al., 2010):

$$Q = k\bar{P}A^{0.85} \quad (5)$$

According to Eq. (2) - (4), fluvial shear stress can be rewritten as (Godard et al., 2010):

$$\tau = \rho g \frac{(QN)^{3/5} S^{7/10}}{W^{3/5}} \quad (6)$$

Therefore, from Eq. (6), we can calculate the fluvial shear stress value after obtaining these necessary parameters.

4.2. Relative parameters calculations

4.2.1. Width (*W*)

The bankfull width of the channels in the study area was mainly measured in the field using distance-measuring equipment (product type Trupulse200B). For places we cannot reach, we used SPOT 5m resolution panchromatic imagery to acquire the bankfull width of the channel. We estimated a relative uncertainty of 5% exists on the resulting width evaluation.

4.2.2. Channel slope (*S*)

The channel network was obtained from a 90 m DEM that is a blend of SRTM (Jarvis et al., 2008). Each river was divided into ~20 segments, each of which has a length of 2 - 4 km. We calculated the average channel slope of each segment, which is equal to the altitude difference of the channel segment divided by the segment length along the channel. We assume a relative uncertainty of 10% on the slope calculations.

4.2.3. Discharge (*Q*)

We acquired 10-year return discharge (Q_{10}) from two monitoring stations (Qin, 2006). The maximum discharge of the Duoyinping station, located on the Qingyi Jiang, was ~1000 m^3/s; the maximum discharge of the Xuankou station on the main channel of Min Jiang was ~1000 m^3/s (Qin, 2006). We assumed that the spatial

variations of precipitation rate are relatively limited over the drainage basin. We related Q_{10} to area A as $Q \propto A^{0.85}$ (Lavé and Avouac, 2001), and acquired the discharge for each survey point along the Qingyi Jiang, Yuxi He, and Shaotang He rivers. For the Q_{10} along the Chu He and Xi He rivers, we assumed that the precipitation rates were similar between the drainage basins of the Qingyi Jiang and Yuxi He rivers. An estimated relative uncertainty of 25% exists on the 10-year return discharge calculations.

4.2.4. Sediments size and roughness coefficient (*N*)

Incising channels in actively-deforming orogenic belts have a large alluvial cover and size distribution of bed sediment. Not only can sediments provide working tools for abrasion to cause bedrock incision, but they also have protection for bedrock (Sklar and Dietrich, 2004). Grain size and sediments supply are fundamental controls on bedrock incision rates (Sklar and Dietrich, 2004). D_{90} is required in fluvial shear stress calculation. We performed bedload counting on photos taken by UAV on typical areas for each surveyed river, and estimated D_{90} for each river. For the roughness coefficient N, we first chose a value of 0.1 for the Shaotang He, to make the fluvial shear stress values in the Pengguan massif similar between the Shaotang He and Min Jiang (Godard et al., 2010). Then we derived the roughness coefficient for other four rivers according to $N \propto D_{90}^{1/6}$ (Chang, 1988; Lavé and Avouac, 2001). The values of D_{90} and N for each river are shown in **Table S1**.

4.3. Individual fluvial shear stress profiles

Fluvial shear stress values of the Qingyi Jiang, Yuxi He, Chu He, Xi He, and Shaotang He rivers are calculated from Eq. (6) along the surveyed streams where relevant parameters were measured (**Figs. 2 & 6**).

The Qingyi Jiang flows through the Proterozoic Baoxing massif, crosses the WYF and flows on the Mesozoic sedimentary units in its lower reach. The fluvial shear stress of the Qingyi Jiang changes markedly across the WYF. The average value in the hanging-wall block of WYF is ~890 Pa; in the footwall, it is ~480 Pa (**Fig. 6a**).

Northward, the Yuxi He is a major tributary of the Qingyi Jiang river basin in the southern Longmen Shan. It crosses the entire Baoxing massif that is bound by the WYF and the SDF, and flows into Mesozoic sedimentary rocks at the range front. The values of fluvial shear stress are somewhat complicated because of both the lithology change and the fault activity. Overall, the river poses greater fluvial shear stress to the hanging-wall of the SDF than its footwall (**Fig. 6b**).

Further north, the Chu He is the main river of a small range frontal catchment drainage. It follows, for several kilometers, along the SDF. With similar lithology on both sides along the SDF, the fluvial shear stress value drops significantly along the SDF, indicating highly fractured rocks caused by fault activity. The average fluvial shear stress value in the hanging-wall and footwall blocks of the SDF are ~ 170 Pa and ~100 Pa, respectively, while it is ~50 Pa along the fault (**Fig. 6c**).

The Xi He presents similar lithologic features to the Chu He. Bedrocks along the river are mainly sandstones and limestones. Although the fluvial shear stress does not

change significantly across the SDF, its value in the hanging-wall block of SDF (~280 Pa) is almost twice that of the footwall block (~150 Pa) (**Fig. 6d**).

The Shaotang He is a major tributary of the Min Jiang. It flows from south to north in the Paleozoic-Triassic rocks, crosses the WMF, flows into the Proterozoic Pengguan massif, and merges into the Min Jiang near the BYF. The average fluvial shear stress in the footwall block of WMF (~ 450 Pa) is higher than that in the hanging-wall (~ 260 Pa), which may be due to lithological contrast: the footwall block mainly contains granitoids whereas the hanging-wall block is covered largely by sandstones (**Fig. 6e**).

4.4. Calibration between fluvial shear stress values and erosion rate

A nondimensional parameter termed Shields stress (τ^*) is an indicator for riverbed mobility, based on reach and cross-sectional average properties (Parker, 1978). It is given by

$$\tau^* = \frac{hS}{(\rho_s/\rho - 1)\, D_{50}} \quad (7)$$

where ρ_s and ρ are density of gravel and water, respectively, D_{50} is the grain diameter not exceeded by 50% (in weight) of the bed load (Lavé and Avouac, 2001). Based on Eqs. (2), (3) and (7), the Shields stress can be written to

$$\tau^* = \frac{\tau}{(\rho_s - \rho)\, g D_{50}} \quad (8)$$

The Shields stress, when exceeds a threshold value, yield a more consistent relationship with the fluvial incision rate than the fluvial shear stress (Lavé and

Avouac, 2001). For same or similar lithology (under similar abrasion), the Shields stress and incision rate (i) have a positive linear correlation (Lavé and Avouac, 2001):

$$i = K(\tau^* - \tau_c^*) \quad (9)$$

where K is erodibility coefficient, mainly related to lithological properties of the bedrock, τ_c^* is the critical Shields stress value for incipient motion. The range of the critical Shields stress is 0.03 to 0.08, depending on shear velocity, D_{50}, and kinematic viscosity of fluid (Neill, 1968; Buffington and Montgomery, 1997).

In this study, a uniform value of D_{50} was selected, because of the similar scale of the rivers and nearly identical tectonic and climatic background. Therefore, a linear relationship between the Shields stress and fluvial shear stress emerges on the basis of Eq. (8), and a positive linear correlation between the fluvial shear stress value and erosion rate is expected. Upon finding this correlation, one can acquire the erosion rates for all survey points (Lavé and Avouac, 2001; Godard et al., 2010). The fluvial shear stress at the segment flowing out of the mountain is usually 1.4 times of the critical value (Paola and Mohrig, 1996; Lavé and Avouac, 2001). We calculated the average fluvial shear stress along the first kilometers downstream of the outlet of the Chu He, Xi He, and Qingyi Jiang rivers, and obtained an average critical fluvial shear stress of ~50 Pa. Then according to Eq. (8) with the critical Shields stress of 0.03-0.08, we derived that D_{50} is 4-10 cm, which is comparable to the D_{50} value (8 cm) estimated by Godard et al. (2010).

We divided the rocks into two groups, granitoid and sedimentary rocks, according to the distinct abrasion rate of rocks in the study area (Godard et al., 2010).

344 Then, we established a linear relationship between the fluvial shear stress value and
345 erosion rate for each rock type (**Fig. 7**). Using average erosion rates from
346 low-temperature thermochronology data, we performed an empirical calibration of the
347 erodibility coefficient in Eq. (9). The denudation rates are equal to the erosion rates in
348 the study area, because no portion of denudation resulted from extensional tectonics
349 here.

350 For river segments in the granitoid rocks, in the hanging-wall of the WYF along
351 the Qingyi Jiang, the average fluvial shear stress is ~800 Pa, and the erosion rate is
352 1-1.5 mm/yr. In the footwall of the WYF along the same river, the values are ~460 Pa
353 and 0.7-0.8 mm/yr, respectively. In the footwall of WMF along the Shaotang He river,
354 ~450 Pa and 0.6-0.7 mm/yr, respectively.

355 For river segments in sedimentary rocks, in the hanging-wall of WMF along the
356 Shaotang He, the average fluvial shear stress is ~260 Pa and the erosion rate is 0.7-0.8
357 mm/yr. In the hanging-wall of the SDF along both the Xi He and the Chu He rivers,
358 ~250 Pa and 0.5-0.6 mm/yr, respectively. The average fluvial shear stress value in the
359 footwall of the SDF along the Xi He and Chu He is ~150 Pa and ~120 Pa,
360 respectively, and the erosion rate is 0.3-0.4 mm/yr for both river segments (**Fig. 7**).

361 We computed weighted regression lines that go through each set of data and the
362 critical fluvial shear stress. The latter has value of ~50 Pa at a zero incision rate and
363 corresponds to the pebble threshold motion (Lavé and Avouac, 2001). Data from the
364 sedimentary rocks and the Precambrian granitoid basement display distinct trends
365 with a slope of 0.0035 and 0.0017, respectively (**Fig. 7**). The newly obtained

empirical erodibility coefficients allowed us to calculate the erosion rates for each survey point on fluvial shear stress, as discussed in section 5.2 below.

5. Discussion

5.1. Reliability of the empirical relationship

The erosion rates obtained in this study show good linear relationship with the fluvial shear stress values in both the granitoid rocks and sedimentary rocks, with $R^2 >$ 0.9. The 2-fold difference between the regression slopes of two rock families are similar to those of Godard et al. (2010), although the slopes (0.0017 and 0.0035) in this study are ~40% higher than those in Godard et al. (2010) (0.0012 and 0.0024, respectively).

We used the denudation rates derived from thermochronology dates only, while Godard et al. (2010) use those from both thermochronology and cosmogenic dates, mainly the later one. Godard et al. (2010) noted that their ^{10}Be-derived erosion rates may be lower than the actual long-term values because their rates (in a time period of ~1.5 ka) may not include the contribution of great earthquakes due to their relative long recurrence intervals (~3 ka) (Ran et al., 2010). Therefore, we suggest that the regression slopes between erosion rate and fluvial shear stress value in this study are more representative for the long-term average erosion in the central and southern Longmen Shan.

Moreover, when the regression slopes of **Fig. 7** are converted to equivalent

erodibility by multiplying a factor of ~1667 (the critical fluvial shear stress of 50 Pa corresponding to the Shields stress of 0.03, and 50/0.03≈1667), the erodibility coefficients of the granitoids and sedimentary rocks in this study are ~2.8 and ~5.8 mm/yr, respectively. They are comparable with the erodibility values (~2 and ~7 mm/yr) converted from the abrasion values by flume experiments (Godard et al., 2010).

In summary, the high R^2 (> 0.9) and the similarity of the erodibility coefficient between the two independent approaches enhance the reliability of the empirical linear relationship between the fluvial shear stress value and erosion rate in this study.

5.2. Spatial pattern of erosion and its implications

5.2.1 Erosion and deformation across the aftershock gap

The new fission track data in this study allow us to document the erosion difference across the range in the aftershock gap, and evaluate the relationship between surface erosion and deep structure. We plotted AFT ages and their corresponding erosion rates in a profile X-X' across the aftershock gap (**Fig. 8**). Five domains of erosion rate exist from the Siguniang pluton in the hinterland to the Sichuan Basin (**Fig. 8**). In the hinterland far from the thrusts, the erosion rate is between 0.1 and 0.5 mm/yr. Approaching the thrust belt, it increases to ~0.7 mm/yr. This is probably an underestimate, as the only AFT age in this domain (~4.9 Ma, Wilson et al., 2011) was ca. 20 km from the WYF (**Fig. 2a**). The erosion rate drops

408 stepwise to 0.5-0.6 mm/yr, then 0.3-0.4 mm/yr, and then zero across the WYF, SDF,
409 and Dayi fault, respectively.

410 We built a crustal-scale section below profile X-X' (**Fig. 8**). All major faults in
411 the X-X' section show reverse faulting, consistent with those to the north and south
412 (Tian et al., 2013; Tan et al., 2014, 2017; Shen et al., 2019). For structures in the
413 shallow crust at the mountain front, we largely adopted the seismic interpretations by
414 Z. Li et al. (2017) on the geometry of the Dayi fault, the Range Front blind thrust
415 (RFBT), and the shallow detachment fault localized in the Triassic in the Sichuan
416 Basin. The hypocenter of the 1970 Dayi earthquake constrained the RFBT geometry
417 down to ~ 14 km. We inferred that the major thrusts (WYF, SDF, and RFBT) have a
418 listric geometry and sole into a sub-horizontal detachment fault/ductile shear zone at
419 ca. 20 km (Hubbard and Shaw, 2009; Tan et al., 2019). Underlying the detachment is
420 a zone of partially molten mid-crust that must have displayed out-of-plane motions
421 (possibly with a dextral sense-of-motion), as inferred from the low-velocity anomalies
422 and orogen-parallel azimuthal anisotropy (e.g., Z. Liu et al., 2018; Bao et al., 2020).
423 We also speculated reverse faulting in the lower crust and across the Moho
424 discontinuity, as detected in the north-central Longmen Shan (Guo et al., 2013; Feng
425 et al., 2016). Depth of the Moho varies from ~58 km under the eastern Tibetan Plateau
426 to ~42 km under the Sichuan Basin, displaying a "Moho ramp" under the southern
427 Longmen Shan (Lu et al., 2019; Tan et al., 2019). The maximum erosion rate in this
428 segment (the aftershock gap) of the Longmen Shan is located in the hanging-wall of
429 WYF (**Fig. 8**), consistent with the "Maximum exhumation belt" along the eastern

Tibetan Plateau margin proposed by Tan et al. (2019).

5.2.2 Along-strike variations in erosion

Below we focus on the spatial variations of erosion between the aftershock gap and surrounding areas. We plotted the erosion rates derived from two independent methods, i.e., low-temperature thermochronology and fluvial shear stress analyses, on the map (for the latter dataset) and in five profiles (for both datasets) (**Fig. 9**).

The thermochronology-derived erosion rates agree well with those derived from fluvial shear stress analysis (**Fig. 9b**). In profile A-A', previous thermochronological studies have revealed an average erosion rate of 0.8-1.2 mm/yr in the hinterland, 0.6-0.7 mm/yr in the hanging-wall block of the BYF, and ~0.2 mm/yr or less at the range front (Godard et al., 2009; Tan et al., 2017; Shen et al., 2019). Profile C-C' shows a similar trend of decreasing erosion rate in different fault blocks: 1.0-1.4 mm/yr in the hanging-wall block of the WYF, 0.7-0.8 mm/yr in its footwall, and less than 0.2 mm/yr at the range front (Arne et al., 1997; Tian et a., 2013; Cook et al., 2013; Tan et al., 2014). The erosion rates obtained by fluvial shear stress are only available for the footwall block of WMF in profile A-A' and the footwall block of WYF in profile C-C'. Their values (0.70 ± 0.25 mm/yr and 0.70 ± 0.24 mm/yr, respectively) are consistent with those obtained by low-temperature thermochronology.

On profile B-B', the AFT age (~4.9 Ma) in the hanging-wall of WYF (Wilson et al., 2011) corresponds to an erosion rate of ~0.7 mm/yr (**Fig. 9b**). This is comparable

452 with the erosion rate of 0.74±0.44 mm/yr calculated from fluvial shear stress. In the
453 footwall block of WYF, the erosion rate obtained from the two AFT ages by this study
454 is 0.5-0.6 mm/yr (**Fig. 5**) and the erosion rate inferred from fluvial shear stress is 0.70
455 ±0.31 mm/yr. The AFT-derived erosion rate in the footwall of SDF is 0.3-0.4 mm/yr
456 (**Fig. 5**), largely agreeing with the 0.28±0.15 mm/yr erosion rate obtained from
457 fluvial shear stress analysis. The erosion rate of 0.3-0.4 mm/yr at the range front of
458 the gap is comparable with the slip rate calculated from seismic reflection profiles (Z.
459 Li et al., 2017).

460 Such a consistency in all three profiles supports previous argument (Liu-Zeng et
461 al., 2011; Z. Li et al., 2016; Y. Liu et al., in review) that the central and southern
462 Longmen Shan has reached a steady-state since the Pliocene.

463 We further plotted two orogen-parallel profiles D-D' and E-E' to portray the
464 along-strike variations in erosion rate between the aftershock gap and adjacent areas
465 (**Fig. 9c**). In the hinterland profile D-D', while elevation is generally higher in the
466 aftershock gap than the adjacent areas, the erosion rate is lower in the gap (**Fig. 9c**).
467 On the contrary, in the range frontal profile E-E', both elevation and erosion rate are
468 greater in the gap. This along-strike variation indicates that the frontal range of the
469 gap undergoes more rapid erosion, and implies that fault activities within the gap are
470 more localized at the mountain front, in comparison with the adjacent areas. This
471 inference is further supported by the latest fault activity based on the deformation of
472 young strata, and the fact that the 1970 M_s 6.2 Dayi earthquake occurred under the
473 range front of the gap (**Figs. 1, 8, & 9a**) (Densmore et al., 2007; H. Wang et al., 2013;

Dong et al., 2017; Shao et al., 2019). If true, this lateral variation in fault activity may be related to the sudden stop of seismic ruptures and distribution of aftershocks in the 2008 Wenchuan and 2013 Lushan earthquakes.

5.3. Mechanism for the aftershock gap: weak material vs. differential erosion

In this section, we evaluate the existing mechanism (weak material) (Z. W. Li et al., 2013; Pei et al., 2014; Liang et al., 2018) and the alternative hypothesis (differential erosion) for the formation of the aftershock gap. Given that the central and southern Longmen Shan thrust belt has reached a steady-state over the past a few Myr (Liu-Zeng et al., 2011; Z. Li et al., 2016), the two models would produce distinct pattern of erosion, which can be tested against aforementioned observations.

Here we use the critical-taper wedge theory to characterize the deformation and earth surface processes in the Longmen Shan thrust belt (Hubbard et al., 2010). The critical-taper wedge theory (Davis et al., 1983; Suppe, 2007) depicts an elegant relationship between the geometry and mechanics of a subaerial, critically-tapered thrust wedge:

$$\alpha + \beta = \frac{\beta + F}{1 + W} \quad (9)$$

where $\boldsymbol{\alpha}$ is surface slope; $\boldsymbol{\beta}$, detachment dip; $\boldsymbol{F}$, detachment fault strength; and $\boldsymbol{W}$, wedge strength.

We follow Y. Liu et al. (in review) to build conceptual wedge models to assess

the competing hypotheses. Consider a three-dimensional, critically-tapered thrust wedge that undergoes uniform shortening, and the central portion represents the aftershock gap. In the "weak material" model, as the wedge strength (W) decreases (due to the presence of mechanically weaker materials) while other variables (i.e., detachment dip, detachment depth, detachment fault strength, and shortening strain) remain unchanged, according to Eq. (9), the surface slope (α) should increase to attain a new, greater taper. The hinterland of the recess (where the wedge strength is reduced) witnesses greater tectonic uplift than do the portions on both sides. In contrast, the frontal part of the wedge at the recess experiences a smaller amount of tectonic uplift than do the adjacent portions. Thereby, along-strike variations in uplift emerge. As the propagation of the deformation front stalls, a recess structure appears (**Fig. 10a**). In a critically-tapered wedge, this results in higher elevation and greater erosion rate at the recess along the hinterland profile F-F' (**Fig. 10b**). In the meantime, it produces lower elevation and smaller erosion rate at the recess along the range-frontal profile G-G' (**Fig. 10c**).

We conduct another "conceptual experiment" on a three-dimensional, critically-tapered thrust wedge for the "differential erosion" model. It also undergoes uniform shortening (**Fig. 10d**). If erosion ($\mathcal{E}$) is reduced in the central portion while other variables remain unchanged along strike, after reaching a new steady-state, the wedge attains the same critical taper everywhere, because the intrinsic properties of the wedge are identical everywhere in this model (Marshak, 2004; Y. Liu et al., in review). Consequently, the central portion of the wedge is more readily to propagate

517 foreland-ward whereas the adjacent portions are prone to stall. A salient forms (**Fig.**
518 **10d**). The surface slope across the salient should be identical with that of the adjacent
519 portions. Hinterland of the salient is expected to gain a higher elevation and display a
520 smaller erosion rate, due to the reduced erosion in this scenario. A cartoon profile H-H'
521 demonstrates such along-strike variations in the hinterland (**Fig. 10e**). At the range
522 front, both elevation and erosion rate at the salient should be slightly greater than
523 those of the adjacent portions, as shown in the cartoon profile J-J' (**Fig. 10f**).

524 The "weak material" model can be represented by the first conceptual
525 experiment (**Fig. 10a**), whereas the "differential erosion" hypothesis corresponds to
526 the latter one (**Fig. 10d**). Based on the results in previous section, the topography and
527 erosion rate patterns predicted by the first model are at odds with the observed
528 patterns at the aftershock gap (**Fig. 10b&c** vs. **Fig. 9c**). On the contrary, predictions of
529 the second model agree well with the observations of topography and erosion rates
530 around the aftershock gap (**Fig. 10e&f** vs. **Fig. 9c**). These comparisons indicate that
531 along-strike variation in erosion could be the main cause for the formation of the
532 aftershock gap and fault segmentation. In other words, due to the heterogeneous,
533 weaker erosion in the hinterland of the gap, deformation in the Longmen Shan thrust
534 wedge propagated to the Sichuan Basin more favorably than its adjacent portions,
535 resulting in the lateral difference of fault activity.

536 The Longmen Shan provides an ideal natural archive to study the erosional
537 influence on tectonics through lateral comparison, thanks to the steep topography,
538 active tectonics, and large rivers that cut through the Longmen Shan. Previous studies

539 (Tan et al., 2018; Y. Liu et al., in review) and this study show that erosion has indeed
540 exerted an important influence on the fault segmentation in the Longmen Shan thrust
541 belt. If all conditions except erosion are uniform in a critically-tapered orogenic
542 wedge, recess emerges in the region with strong erosion (Marshak, 2004). The
543 Dujiangyan recess in the central Longmen Shan is proposed to be such a recess
544 controlled by lateral differential erosion (Y. Liu et al., in review). This mechanism on
545 the surface also affected the coseismic slip during the 2008 Wenchuan earthquake
546 (Tan et al., 2018). Therefore, in an orogenic belt with strong erosion such as the
547 Longmen Shan, along-strike variations in structural geometry, although sometimes
548 used as a mark for multi-stage deformation, could be simply controlled by the lateral
549 difference of erosion. One shall not ignore the erosional impact.
550

551 ## 5.4. Implication for seismicity: Asperity model vs. Barrier model

552 Paleoseismology studies suggest that earthquakes recurrent on a given fault may
553 often have characteristic length and amount of slip (e.g., Wallace, 1981; Sieh, 1981;
554 Wesnousky et al., 1982). Asperity model and barrier model have been raised up to
555 explain this phenomenon (Aki, 1984). Both terms, “asperity” and “barrier”, refer to
556 strong patches on fault surfaces that resist breaking. However, the roles of strong
557 patches in the rupture process are distinctly different (**Fig. 11a&b**) (Aki, 1984). In the
558 asperity model, the fault plane contains a strong patch surrounded by a slip-released
559 region before an earthquake, and stress becomes homogeneous after an earthquake

560 (**Fig. 11a**). In the barrier model, the fault plane is uniformly stressed before an
561 earthquake, and it contains unbroken strong patches in postseismic stage (**Fig. 11b**).
562 The competing hypotheses for the aftershock gap in Longmen Shan correspond
563 to the two theoretical models. The weak material hypothesis argues that the fault
564 plane in the gap undergoes ductile deformation and are hardly stressed, which
565 matches the asperity model (**Fig. 11a**). The differential erosion hypothesis, on the
566 other hand, mimics the barrier model (**Fig. 11b**). It considers the fault block between
567 the BYF and WYF as a stress barrier, because of the high topography within the gap.
568 Shortening across the gap are accommodated by the thrust faults in the foreland
569 region (**Fig. 11c**). According to the aforementioned analyses, the barrier model may
570 better explain the characteristic earthquake appearance in the Longmen Shan (e.g.,
571 Ran et al., 2010). The active faults at the range front area within the gap, therefore,
572 imposes high seismic risks to the region. This is remarkably different from the seismic
573 assessment based on the asperity model. Our inference agrees with Z. Li et al. (2017),
574 who alerted the potential of great earthquakes at the range front of the southern
575 Longmen Shan. While trenches on the SDF within the aftershock gap had revealed
576 several paleo-earthquakes over the past 3000 years, which may have reduced the
577 recent earthquake risk on this fault (H. Wang et al., 2015; Dong et al., 2017; Shao et
578 al., 2019), the potential risk on other active faults should not be overlooked.
579

580 # 6. Conclusions

581 We have proposed an alternative explanation for the aftershock gap in the

582 southern Longmen Shan, eastern Tibetan Plateau margin: differential erosion induced
583 along-strike variations in fault activity. To testify the new explanation and pre-exist
584 explanation (weak material), we have studied the spatial distribution of erosion at the
585 aftershock gap of the Longmen Shan, based on low-temperature thermochronology
586 and fluvial shear stress analysis. We draw the following conclusions:

587 (1) We have reported eight apatite fission track dates within the aftershock gap: ~6-44
588 Ma. Our modeling revealed that the erosion rate of the fault block between WYF
589 and SDF is 0.5-0.6 mm/yr, while the footwall of the SDF is 0.3-0.4 mm/yr, since
590 ~8 Ma.

591 (2) We have calculated the erosion rate for ~800 survey points of fluvial shear stress
592 along five rivers around the aftershock gap, based on the empirical relationship
593 between the fluvial shear stress and erosion rate.

594 (3) Along-strike variations in erosion rate and topography exist in the aftershock gap.
595 In the hinterland, while elevation is generally higher in the gap than the adjacent
596 areas, the erosion rate is lower in the gap. Along the range front, both elevation
597 and erosion rate are greater in the gap.

598 (4) We have built two conceptual critical-taper wedge models to evaluate the “weak
599 material” and “differential erosion” hypotheses. Comparison between model
600 predictions and our observations strongly favors the differential erosion as the
601 main cause for the aftershock gap and fault segmentation.

602 (5) This study implies that the aftershock gap in the southern Longmen Shan is not a
603 ductile deformation zone, but a barrier for the rupture during the 2008 Wenchuan

604 earthquake, which needs serious consideration for seismic risk assessment.

605

606 Acknowledgments

607 This study is supported by the Integrated Study on Seismotectonic Models for
608 Typical Regions of China Earthquake Administration (grant number F-18-04), and the
609 GURI Fund from the State of Texas and the University of Houston. We thank Fang
610 Xu for her help in fieldwork. The topography data (SRTM data V4) is from the
611 website (http://srtm.csi.cgiar.org). The data of aftershock of the 2008 Wenchuan
612 earthquake is from Huang et al. (2008). The data of aftershock of the 2013 Lushan
613 earthquake is from Fang et al. (2013). The rock abrasion data are from Godard et al.
614 (2010). The data in Tables S1 is publicly available
615 (https://doi.org/10.5281/zenodo.3739423).

616

617

618 References

619 Arne, D., Worley, B., Wilson, C., Chen, S. F., & Dirks, P. (1997). Differential
620 exhumation in response to episodic thrusting along the eastern margin of the
621 tibetan plateau. *Tectonophysics, 280*(3-4), 239-256.
622 Arrowsmith, J. R., & Strecker, M. R. (1999). Seismotectonic range-front
623 segmentation and mountain-belt growth in the Pamir-Alai region, Kyrgyzstan
624 (India-Eurasia collision zone). *Geological Society of America Bulletin, 111*(111),
625 1665-1683.
626 Avouac, J. P., & Burov, E. B. (1996). Erosion as a driving mechanism of
627 intracontinental mountain growth. *Journal of Geophysical Research: Solid Earth,*
628 *101*(B8).

Bao, X., Song, X., Eaton, D. W., Xu, Y., & Chen, H. (2020). Episodic lithospheric deformation in eastern Tibet inferred from seismic anisotropy. *Geophysical Research Letters*, *47*(3), e2019GL085721.

Brandon, M. T., Roden-Tice, M. K., & Garver, J. I. (1998). Late Cenozoic exhumation of the Cascadia accretionary wedge in the Olympic Mountains, northwest Washington State. *Geological Society of America Bulletin*, *110*(8), 985-1009.

Burchfiel, B. C., Zhiliang, C., Yupinc, L., & Royden, L. H. (1995). Tectonics of the Longmen Shan and adjacent regions, central China. *International Geology Review*, *37*(8), 661-735.

Buffington, J. M., & Montgomery, D. R. (1997). A systematic analysis of eight decades of incipient motion studies, with special reference to gravel-bedded rivers. *Water Resources Research*, *33*(8), 1993-2029.

Burchfiel, B. C., Zhiliang, C., Yupinc, L., & Royden, L. H. (1995). Tectonics of the Longmen Shan and adjacent regions, Central China. *International Geology Review*, *37*(8), pp.661-735.

Chang, H. H. (1988). *Fluvial processes in river engineering*: Malabar, Fla.

Chen, S. F., Wilson, C. J. L., Deng, Q. D., Zhao, X. L., & Zhi, L. L. (1994). Active faulting and block movement associated with large earthquakes in the Min Shan and Longmen Mountains, northeastern Tibetan Plateau. *Journal of Geophysical Research: Solid Earth*, *99*(B12), 24025-24038.

Clark, M. K., & Royden, L. H. (2000). Topographic ooze: Building the eastern margin of Tibet by lower crustal flow. *Geology*, *28*(8), 703-706.

Calais, E., Freed, A. M., Arsdale, R. V., & Stein, S. (2010). Triggering of new Madrid seismicity by late-pleistocene erosion. *Nature*, *466*(7306), P.608-611.

Cook, K. L., Royden, L. H., Burchfiel, B. C., Lee, Y. H., & Tan, X. (2013). Constraints on Cenozoic tectonics in the southwestern Longmen Shan from low-temperature thermochronology. *Lithosphere*, *5*(4), 393-406.

Davis, D., Suppe, J., & Dahlen, F. A. (1983). Mechanics of fold-and-thrust belts and accretionary wedges. *Journal of Geophysical Research: Solid Earth*, *88*(B2), 1153-1172.

Densmore, A. L., Ellis, M. A., Li, Y., Zhou, R., Hancock, G. S., & Richardson, N. (2007). Active tectonics of the Beichuan and Pengguan faults at the eastern margin of the Tibetan Plateau. *Tectonics*, *26*(4).

de Sigoyer, J., Vanderhaeghe, O., Duchêne, S., & Billerot, A. (2014). Generation and emplacement of Triassic granitoids within the Songpan Ganze accretionary-orogenic wedge in a context of slab retreat accommodated by tear faulting, Eastern Tibetan plateau, China. *Journal of Asian Earth Sciences*, *88*, 192-216.

Donelick, R. A., O'Sullivan, P. B., & Ketcham, R. A. (2005). Apatite fission-track

668 dating. *Reviews in Mineralogy & Geochemistry*, 527-565.
669 Dong, S. P., Han, Z. J., & An, Y. F. (2017). Paleoseismological events in the “seismic
670 gap” between the 2008 Wenchuan and the 2013 Lushan earthquakes and
671 implications for future seismic potential. *Journal of Asian Earth Sciences*, *135*,
672 1-15.
673 Ehlers, T. A. (2005). Crustal thermal processes and the interpretation of
674 thermochronometer data. *Reviews in Mineralogy and Geochemistry*, *58*(1),
675 315-350.
676 Fang, L., Wu, J., Wang, W., Du, W., Su, J., Wang, C., ... & Cai, Y. (2015). Aftershock
677 observation and analysis of the 2013 Ms7.0 Lushan earthquake. *Seismological*
678 *Research Letters*, *86*(4), 1135-1142.
679 Fang, L., Jianping, W. U., Weilai, W., Zuoyong, L., Changzai, W., & Ting, Y., et al.
680 (2013). Relocation of the mainshock and aftershock sequences of Ms7.0 Sichuan
681 Lushan earthquake. *Chinese Science Bulletin*, *058*(028), 3451-3459.
682 Gan, W., Zhang, P., Shen, Z. K., Niu, Z., Wang, M., Wan, Y., ... & Cheng, J. (2007).
683 Present-day crustal motion within the Tibetan Plateau inferred from GPS
684 measurements. *Journal of Geophysical Research: Solid Earth*, *112*(B8).
685 Godard, V., Pik, R., Lavé, J., Cattin, R., Tibari, B., De Sigoyer, J., ... & Zhu, J. (2009).
686 Late Cenozoic evolution of the central Longmen Shan, eastern Tibet: insight
687 from (U-Th)/He thermochronometry. *Tectonics*, *28*(5).
688 Godard, V., Lavé, J., Carcaillet, J., Cattin, R., Bourlès, D., & Zhu, J. (2010). Spatial
689 distribution of denudation in Eastern Tibet and regressive erosion of plateau
690 margins. *Tectonophysics*, *491*(1-4), 253-274.
691 Green, P. F. (1985). Comparison of zeta calibration baselines for fission-track dating
692 of apatite, zircon and sphene. *Chemical Geology: Isotope Geoscience section*,
693 *58*(1-2), 1-22.
694 Horton, B. K. (1999). Erosional control on the geometry and kinematics of thrust belt
695 development in the central Andes. *Tectonics*, *18*(6), 1292-1304.
696 Huang, Y., Wu, J., Zhang, T., & Zhang, D. (2008). Relocation of the M8.0 Wenchuan
697 earthquake and its aftershock sequence. *Science in China Series D: Earth*
698 *Sciences*, *51*(12), 1703-1711.
699 Hubbard, J., & Shaw, J. H. (2009). Uplift of the Longmen Shan and Tibetan plateau,
700 and the 2008 Wenchuan (M= 7.9) earthquake. *Nature*, *458*(7235), 194-197.
701 Hubbard, J., Shaw, J. H., & Klinger, Y. (2010). Structural Setting of the 2008 Mw 7.9
702 Wenchuan, China, EarthquakeStructural Setting of the 2008 Mw 7.9 Wenchuan,
703 China, Earthquake. *Bulletin of the Seismological Society of America*, *100*(5B),
704 2713-2735.
705 Hurford, A. J., & Green, P. F. (1983). The zeta age calibration of fission-track dating.
706 *Chemical Geology*, *41*, 285-317.

Jarvis, A., Reuter, H. I., Nelson, A., & Guevara, E. (2008). Hole-filled SRTM for the globe Version 4. *available from the CGIAR-CSI SRTM 90m Database (http://srtm. csi. cgiar. org)*, *15*, 25-54.

Jia, D., Wei, G., Chen, Z., Li, B., Zeng, Q., & Yang, G. (2006). Longmen Shan fold-thrust belt and its relation to the western Sichuan Basin in central China: New insights from hydrocarbon exploration. *AAPG Bulletin*, *90*(9), 1425-1447.

Jin, W., Tang, L., Yang, K., Wan, G., & Lü, Z. (2010). Segmentation of the Longmen Mountains thrust belt, western Sichuan foreland basin, SW China. *Tectonophysics*, *485*(1-4), 107-121.

Ketcham, R. A., Carter, A., Donelick, R. A., Barbarand, J., & Hurford, A. J. (2007). Improved measurement of fission-track annealing in apatite using c-axis projection. *American Mineralogist*, *92*(5-6), 789-798.

Kirby, E., Reiners, P. W., Krol, M. A., Whipple, K. X., Hodges, K. V., Farley, K. A., ... & Chen, Z. (2002). Late Cenozoic evolution of the eastern margin of the Tibetan Plateau: Inferences from 40Ar/39Ar and (U-Th)/He thermochronology. *Tectonics*, *21*(1), 1-1.

Lavé, J., & Avouac, J. P. (2001). Fluvial incision and tectonic uplift across the Himalayas of central Nepal. *Journal of Geophysical Research: Solid Earth*, *106*(B11), 26561-26591.

Li, Z., Liu-Zeng, J., Jia, D., Sun, C., Wang, W., Yuan, Z., & Liu, B. (2016). Quaternary activity of the range front thrust system in the Longmen Shan piedmont, China, revealed by seismic imaging and growth strata. *Tectonics*, *35*(12), 2807-2827.

Li, Z., Liu-Zeng, J., Almeida, R., Hubbard, J., Sun, C., & Yi, G. (2017). Re-evaluating seismic hazard along the southern Longmen Shan, China: Insights from the 1970 Dayi and 2013 Lushan earthquakes. *Tectonophysics*, *717*, 519-530.

Li, Z. W., Tian, B., Liu, S., & Yang, J. (2013). Asperity of the 2013 Lushan earthquake in the eastern margin of Tibetan Plateau from seismic tomography and aftershock relocation. *Geophysical Journal International*, *195*(3), 2016-2022.

Liu, T. K., Hsieh, S., Chen, Y. G., & Chen, W. S. (2001). Thermo-kinematic evolution of the Taiwan oblique-collision mountain belt as revealed by zircon fission track dating. *Earth and Planetary Science Letters*, *186*(1), 45-56.

Liu, Z., Liang, C., Hua, Q., Li, Y., Yang, Y., He, F., & Fang, L. (2018). The seismic potential in the seismic gap between the Wenchuan and Lushan earthquakes revealed by the joint inversion of receiver functions and ambient noise data. *Tectonics*, *37*(11), 4226-4238.

Liu-Zeng, J., Zhang, Z., Wen, L., Tapponnier, P., Sun, J., Xing, X., Hu, G., Xu, Q., Zeng, L., Ding, L. and Ji, C. (2009). Co-seismic ruptures of the 12 May 2008, Ms

746 8.0 Wenchuan earthquake, Sichuan: East–west crustal shortening on oblique,
747 parallel thrusts along the eastern edge of Tibet. *Earth and Planetary Science*
748 *Letters*, *286*(3-4), 355-370.
749 Liu-Zeng, J., Wen, L., Oskin, M., & Zeng, L. (2011). Focused modern denudation of
750 the Longmen Shan margin, eastern Tibetan Plateau. *Geochemistry, Geophysics,*
751 *Geosystems*, *12*(11).
752 Lu, R., He, D., John, S., Wu, J.E., Liu, B. and Chen, Y., (2014). Structural model of
753 the central Longmen Shan thrusts using seismic reflection profiles: Implications
754 for the sediments and deformations since the Mesozoic. *Tectonophysics*, *630*,
755 pp.43-53.
756 Lu, R., Liu, Y., Xu, X., Tan, X., He, D., Yu, G., ... & Wu, X. (2019). Three-
757 dimensional model of the lithospheric structure under the eastern Tibetan Plateau:
758 Implications for the active tectonics and seismic hazards. *Tectonics*, *38*(4),
759 1292-1307.
760 Marshak, S. (2004). Salients, recesses, arcs, oroclines, and syntaxes: A review of ideas
761 concerning the formation of map-view curves in fold-thrust belts. In: K. R.
762 McClay ed., Thrust tectonics and hydrocarbon systems, *AAPG Memoir*, 82,
763 131-156.
764 Mazzoli, S., Pierantoni, P. P., Borraccini, F., Paltrinieri, W., & Deiana, G. (2005).
765 Geometry, segmentation pattern and displacement variations along a major
766 Apennine thrust zone, central Italy. *Journal of Structural Geology*, *27*(11),
767 1940-1953.
768 Naeser, C. W., Zimmermann, R. A., & Cebula, G. T. (1981). Fission-track dating of
769 apatite and zircon: an interlaboratory comparison. *Nuclear Tracks*, *5*(1-2), 65-72.
770 Norris, R. J., & Cooper, A. F. (1997). Erosional control on the structural evolution of a
771 transpressional thrust complex on the Alpine Fault, New Zealand. *Journal of*
772 *Structural Geology*, *19*(10), 1323-1342.
773 Pei, S., Zhang, H., Su, J., & Cui, Z. (2014). Ductile gap between the Wenchuan and
774 Lushan earthquakes revealed from the two-dimensional Pg seismic tomography.
775 *Scientific Reports*, *4*(1), 1-6.
776 Qin, J., Huh, Y., Edmond, J. M., Du, G., & Ran, J. (2006). Chemical and physical
777 weathering in the Min Jiang, a headwater tributary of the Yangtze River.
778 *Chemical Geology*, *227*(1-2), 53-69.
779 Richardson, N. J., Densmore, A. L., Seward, D., Fowler, A., Wipf, M., Ellis, M. A., ...
780 & Zhang, Y. (2008). Extraordinary denudation in the Sichuan Basin: Insights
781 from low-temperature thermochronology adjacent to the eastern margin of the
782 Tibetan Plateau. *Journal of Geophysical Research: Solid Earth*, *113*(B4).
783 Royden, L. H., Burchfiel, B. C., King, R. W., Wang, E., Chen, Z., Shen, F., & Liu, Y.
784 (1997). Surface deformation and lower crustal flow in eastern Tibet. *Science*,

785 *276*(5313), 788-790.
786 Shi, F., He, H. L., & Wei, Z. Y. (2012). Coseismic horizontal shortening associated
787 with the 2008 Wenchuan earthquake along the Baishahe segment from high
788 resolution satellite images. *Journal of Asian Earth Sciences*, 50, p.164-170.
789 Shao, C., Liu, S., Li, Y., Zhou, R., Wang, S., Long, J., ... & Yan, M. (2019).
790 Paleoseismic events on the Shuangshi-Dachuan fault of the seismic gap,
791 Longmen Shan thrust belt, eastern margin of the Tibetan Plateau. *Journal of*
792 *Asian Earth Sciences*, *169*, 1-10.
793 Shen, X., Tian, Y., Zhang, G., Zhang, S., Carter, A., Kohn, B., Vermeesch, P., Liu, R.
794 and Li, W., (2019). Late Miocene hinterland crustal shortening in the Longmen
795 Shan thrust belt, the eastern margin of the Tibetan Plateau. *Journal of*
796 *Geophysical Research: Solid Earth*, *124*(11), pp.11972-11991.
797 Shen, Z. K., Sun, J., Zhang, P., Wan, Y., Wang, M., Bürgmann, R., ... & Wang, Q.
798 (2009). Slip maxima at fault junctions and rupturing of barriers during the 2008
799 Wenchuan earthquake. *Nature Geoscience*, *2*(10), 718-724.
800 Sklar, L. S., & Dietrich, W. E. (2004). A mechanistic model for river incision into
801 bedrock by saltating bed load. *Water Resources Research*, *40*(6).
802 Snyder, N. P., Whipple, K. X., Tucker, G. E., & Merritts, D. J. (2000). Landscape
803 response to tectonic forcing: DEM analysis of stream profiles in the Mendocino
804 triple junction region, northern California. *Geological Society of America*
805 *Bulletin*, *112*(8), 1250-1263.
806 Sun, C., Jia, D., Yin, H., Chen, Z., Li, Z., Shen, L., et al. (2016). Sandbox modeling of
807 evolving thrust wedges with different preexisting topographic relief: Implications
808 for the Longmen Shan thrust belt, eastern Tibet. *Journal of Geophysical*
809 *Research: Solid Earth*, 121, 4591–4614.https://doi.org/10.1002/2016JB013013
810 Sun, C., Li, Z., Zheng, W., Jia, D., Zhang, D., Fan, X., & Zhang, P. (2019). 3D
811 geometry of range front blind ramp and its effects on structural segmentation of
812 the southern Longmen Shan front, eastern Tibet. *Journal of Asian Earth Sciences*,
813 *181*, 103911.
814 Sun, M., Yin, A., Yan, D., Ren, H., Mu, H., Zhu, L., & Qiu, L. (2018). Role of
815 pre-existing structures in controlling the Cenozoic tectonic evolution of the
816 eastern Tibetan plateau: New insights from analogue experiments. *Earth and*
817 *Planetary Science Letters*, *491*, 207-215.
818 Suppe, J. (2007). Absolute fault and crustal strength from wedge tapers. *Geology*,
819 *35*(12), 1127-1130.
820 Tan, X. B., Lee, Y. H., Chen, W. Y., Cook, K. L., & Xu, X. W. (2014). Exhumation
821 history and faulting activity of the southern segment of the Longmen Shan,
822 eastern Tibet. *Journal of Asian Earth Sciences*, *81*, 91-104.
823 Tan, X. B., Xu, X. W., Lee, Y. H., Lu, R. Q., Liu, Y., Xu, C., ... & Kang, W. J. (2017).

824 Late Cenozoic thrusting of major faults along the central segment of Longmen
825 Shan, eastern Tibet: Evidence from low-temperature thermochronology.
826 *Tectonophysics*, *712*, 145-155.
827 Tan, X., Yue, H., Liu, Y., Xu, X., Shi, F., Xu, C., Ren, Z., Shyu, J.B.H., Lu, R. and
828 Hao, H., (2018). Topographic loads modified by fluvial incision impact fault
829 activity in the Longmenshan thrust belt, eastern margin of the Tibetan Plateau.
830 *Tectonics*, *37*(9), pp.3001-3017.
831 Tan, X., Liu, Y., Lee, Y. H., Lu, R., Xu, X., Suppe, J., ... & Xu, C. (2019). Parallelism
832 between the maximum exhumation belt and the Moho ramp along the eastern
833 Tibetan Plateau margin: Coincidence or consequence? *Earth and Planetary*
834 *Science Letters*, *507*, 73-84.
835 Tapponnier, P., Zhiqin, X., Roger, F., Meyer, B., Arnaud, N., Wittlinger, G., & Jingsui,
836 Y. (2001). Oblique stepwise rise and growth of the Tibet Plateau. *Science*,
837 *294*(5547), 1671-1677.
838 Tian, Y., Kohn, B. P., Gleadow, A. J., & Hu, S. (2013). Constructing the Longmen
839 Shan eastern Tibetan Plateau margin: Insights from low-temperature
840 thermochronology. *Tectonics*, *32*(3), 576-592.
841 Xu, G., & Kamp, P. J. (2000). Tectonics and denudation adjacent to the Xianshuihe
842 Fault, eastern Tibetan Plateau: Constraints from fission track thermochronology.
843 *Journal of Geophysical Research: Solid Earth*, *105*(B8), 19231-19251.
844 Xu, X., Wen, X., Yu, G., Chen, G., Klinger, Y., Hubbard, J., & Shaw, J. (2009).
845 Coseismic reverse-and oblique-slip surface faulting generated by the 2008 Mw
846 7.9 Wenchuan earthquake, China. *Geology*, *37*(6), 515-518.
847 Xu, X., Wen, X., Han, Z., Chen, G., Li, C., Zheng, W., ... & Wei, Z. (2013). Lushan M
848 S 7.0 earthquake: A blind reserve-fault event. *Chinese Science Bulletin*,
849 *58*(28-29), 3437-3443.
850 Yin, A., & Harrison, T. M. (2000). Geologic evolution of the Himalayan-Tibetan
851 orogen. *Annual Review of Earth and Planetary Sciences*, *28*(1), 211-280.
852 Wang, E., Kirby, E., Furlong, K. P., Van Soest, M., Xu, G., Shi, X., ... & Hodges, K. V.
853 (2012). Two-phase growth of high topography in eastern Tibet during the
854 Cenozoic. *Nature Geoscience*, *5*(9), 640-645.
855 Wagner, G., & Van den Haute, P. (2012). *Fission-track dating* (Vol. 6). Springer
856 Science & Business Media.
857 Willett, S.D. (1997). Inverse modeling of annealing of fission tracks in apatite; 1, A
858 controlled random search method. *American Journal of Science*, *297*(10),
859 pp.939-969.
860 Wilson, C. J., & Fowler, A. P. (2011). Denudational response to surface uplift in east
861 Tibet: Evidence from apatite fission-track thermochronology. *Bulletin*, *123*(9-10),
862 1966-1987.

Zheng, G., Wang, H., Wright, T. J., Lou, Y., Zhang, R., Zhang, W., ... & Wei, N. (2017). Crustal deformation in the India-Eurasia collision zone from 25 years of GPS measurements. *Journal of Geophysical Research: Solid Earth*, *122*(11), 9290-9312.

Zheng, Y., Ma, H., Lü, J., Ni, S., Li, Y., & Wei, S. (2009). Source mechanism of strong aftershocks (Ms⩾ 5.6) of the 2008/05/12 Wenchuan earthquake and the implication for seismotectonics. *Science in China Series D: Earth Sciences*, *52*(6), 739-753.

Figure captions

Figure 1. Topographic map and neotectonic setting of the Longmen Shan, eastern margin of Tibetan Plateau. Distribution of aftershocks of the 2008 Wenchuan earthquake (red circles) and the 2013 Lushan earthquake (yellow circles) are from Huang et al. (2008) and Fang et al. (2013), respectively. Epicenters (with focal mechanism solutions, if available) for five major earthquakes from Z. Li et al. (2017) and references therein. The aftershock gap is bounded by dark blue dashed lines. Light blue curves denote rivers. Note the relative high topography in the aftershock gap. Surface rupture of the 2008 Wenchuan earthquake from Xu et al. (2009). Abbreviations: BYF, Beichuan-Yingxiu fault; DYF, Dayi fault; JGF, Jiangyou-Guanxian fault; SDF, Shuangshi-Dachuan fault; WMF, Wenchuan-Maoxian fault; WYF, Wulong-Yanjing fault; XPF, Xiongpo fault; XSHF, Xianshuihe fault.

Figure 2. (a) Topographic map of the central and southern Longmen Shan, and low-temperature thermochronology data from literature and this study. Data sources: (1) Tan et al. (2017); (2) E. Wang et al. (2012); (3) Kirby et al. (2002); (4) Richardson et al. (2008); (5) Arne et al. (1997); (6) Wilson et al. (2011); (7) Tan et al. (2014); (8) Xu et al. (2000); (9) Tian et al. (2013); (10) Cook et al. (2013); (11) Godard et al. (2009); (12) Shen et al. (2019). (b) Geological map of the central and southern Longmen Shan, and distribution of fluvial shear stress calculations (dark blue lines along rivers). Abbreviations: AFT, apatite fission track; ZFT, zircon fission track; AHe, apatite (U-Th)/He; ZHe, zircon (U-Th)/He; BM, Baoxing massif; PM, Pengguan massif; XM, Xuelongbao massif; SP, Siguniang pluton. For selective period and epoch: Z, Sinian (late Neoproterozoic); $T_{1\text{-}2}$, Lower and Middle Triassic; T_3, Upper Triassic; E, Neogene.

Figure 3. Age histograms and radial plots for the AFT samples. For each sample, the pooled age and the number of grains counted are indicated on the histogram.

Figure 4. Thermal modeling (left) and track length distributions (right) for DY-07, 08, and 14. In left panel, purple envelope represents good fit paths; green envelope represents acceptable fit paths; black thick line denotes weighted mean path; and black boxes are constraint for modeling. Yellow box highlights the rapid cooling since 8 Ma. Thermal history in grey shadow shall be ignored due to no constraint in the annealing zone. In right panel, green lines denote track length distribution of best-fit modeled thermal history. GOF: Goodness of fit.

Figure 5. Close-up view of thermal history from 20 Ma to present, compared with modeled thermal histories with constant denudation rate. Curves of DY-07, 08, and 14 are weighted mean paths of their thermal history shown in **Fig. 4**, while those of the DY-01 and 04 are based on the dates and closure temperature. Cooling histories of rocks with denudation rate of 0.3, 0.4, 0.5 and 0.6 mm/yr since 8 Ma are modeled by TERRA software (Ehlers, 2005), with boundary conditions below: surface temperature, 20°C; basal temperature gradient, 25°C/km; maximum model depth, 50 km; and diffusivity, $1.3636*10^{-6}$ m^2/s.

Figure 6. Compilation of river elevation, flood discharge, width, abrasion, and fluvial shear stress with cumulative uncertainty (dark grey area), along the (a) Qingyi Jiang, (b) Yuxi He, (c) Chu He, (d) Xi He, and (e) Shaotang He. The abrasion rates for each formation are from Godard et al. (2010). An index map of rivers and faults in the study area is shown in the lower-right corner.

Figure 7. Comparison of basin-averaged fluvial shear stress values and erosion rate from thermochronology measurement. Dashed lines indicate the best linear weighted fits through alluvial sands data for the granitoid crystalline basement (1) and the Paleozoic-Mesozoic sedimentary units (2). The linear fits go through the critical fluvial shear stress value of ~50 Pa. Data point from the hanging-wall block of WMF along the Somang Qu is from Godard et al. (2010). Other data from this study. HW, hanging-wall; FW, footwall.

Figure 8. Erosion rates derived from AFT data and modeling (upper panel) and a schematic crustal-scale sectionX-X' (lower panel) across the aftershock gap. See **Fig. 2b** for X-X' location. Black points denote AFT samples. Data sources: Xu et al. (2000), Wilson et al. (2011), Tan et al. (2014), and this study. Upper crustal structures are adapted from Hubbard and Shaw (2009) and Z. Li et al. (2017). The Mesozoic Siguniang pluton (SP) is not differentiated from the Precambrian crystalline basement due to unconstrained subsurface boundaries. The partially molten mid-crust (pink) with out-of-plane motion is drawn according to Bao et al. (2020). Thrust faults in the lower crust (grey, dashed lines) are schematic, adapted from Guo et al. (2013) and Feng et al. (2016). Depths of the Moho from Lu et al. (2019). Abbreviations: Cz, Cenozoic; Mz, Mesozoic; Pz, Paleozoic. No vertical exaggeration.

Figure 9. Spatial distribution of denudation and topography in the study area. (a) Topographic map and plot of erosion rates along river segments after calibration from **Fig. 7**. (b) Topography profiles (left y-axis) and erosion distribution (right y-axis) along A-A', B-B' and C-C' swath profiles across the Longmen Shan. Green box shows range of average erosion rate inferred from low-temperature thermochronology. Data source: (I) Tan et al. (2017) and Shen et al. (2019); (II) Godard et al. (2009); (III) Tan et al. (2017); (IV) Wilson et al. (2011); (V) and (VI) this study; (VII) Tian et al. (2013) and Tan et al. (2014); (VIII) Cook et al. (2013) and Tan et al. (2014); (IX) Arne et al.

(1997). Red line and semi-transparent red box denote average erosion rate from calibration of fluvial shear stress with error range (±1σ). (c) Topography and erosion rate distribution along the D-D' and E-E' swath profiles (2 km at each side). Dashed and solid thick lines denote variation tendency of erosion and elevation, respectively.

Figure 10. Competing models and their predictions for the formation of the aftershock gap. Revised from Y. Liu et al. (in review). (a) Differential wedge strength model. (b) and (c) show patterns of predicted elevation and erosion rate along profiles F-F' and G-G', respectively. As we assume uniform erosion capacity, the erosion rate is positive correlated with the uplift rate. See (a) for profile locations. (d) Differential erosion rate model. (e) and (f) show patterns of predicted elevation and erosion rate along profiles H-H' and J-J' profiles, respectively. See (d) for profile locations.

Figure 11. (a) Asperity model. (b) Barrier model. Both revised from Aki (1984). Shaded region is stressed, and blank region is slipped. (c) Sketch map for the active faults and barriers in the central and southern Longmen Shan. Red lines are active faults, and the black lines are inactive or weakly active faults, which act as barrier in earthquakes.

Figure 1.

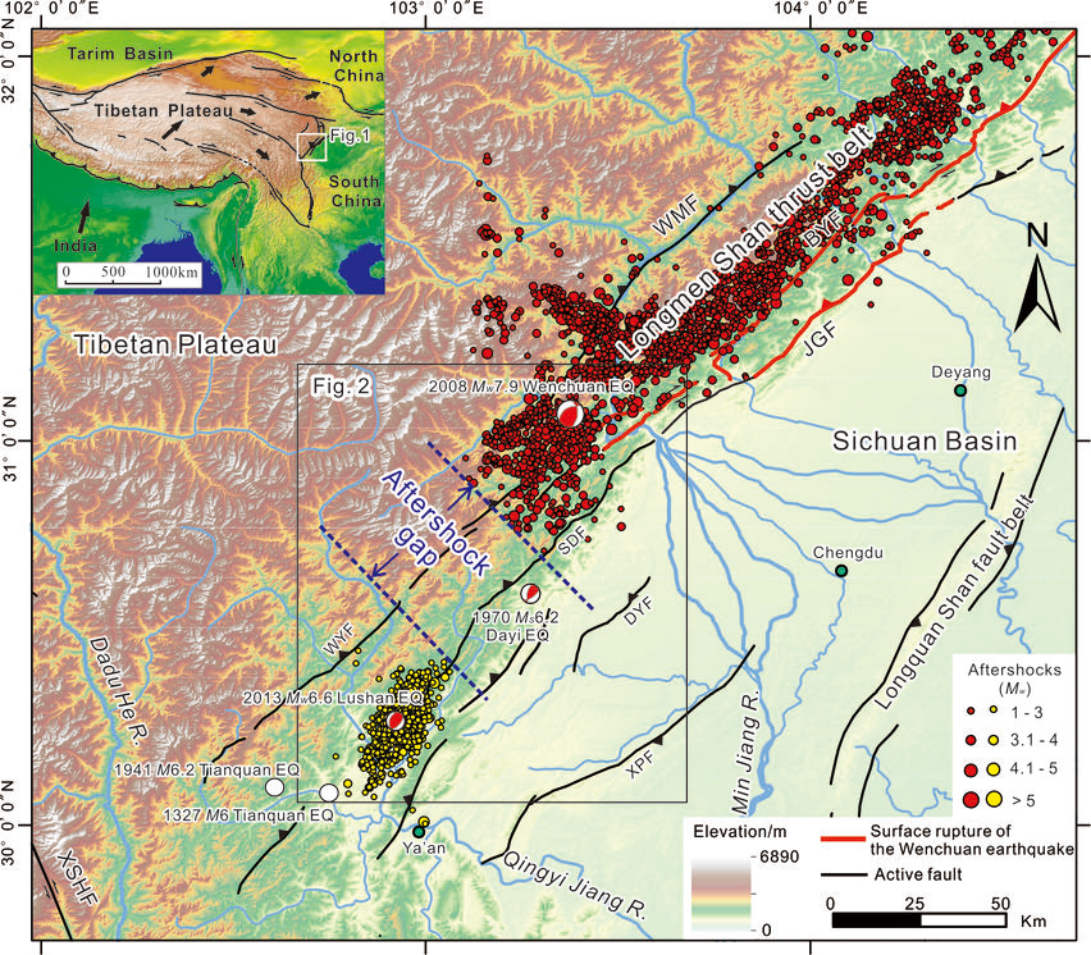
102° 0′ 0″E
103° 0′ 0″E
104° 0′ 0″E
32° 0′ 0″N
31° 0′ 0″N
30° 0′ 0″N
Tarim Basin
North China
Tibetan Plateau
Fig.1
South China
India
0 500 1000km
Tibetan Plateau
Fig. 2
Longmen Shan thrust belt
WMF
BYF
JGF
2008 Mw7.9 Wenchuan EQ
Aftershock gap
SDF
1970 Ms6.2 Dayi EQ
DYF
WYF
2013 Mw6.6 Lushan EQ
1941 M6.2 Tianquan EQ
1327 M6 Tianquan EQ
XSHF
XPF
Dadu He R.
Min Jiang R.
Qingyi Jiang R.
Ya'an
Deyang
Sichuan Basin
Chengdu
Longquan Shan fault belt
N
Aftershocks (Mw)
1 - 3
3.1 - 4
4.1 - 5
> 5
Elevation/m
6890
0
Surface rupture of the Wenchuan earthquake
Active fault
0 25 50
Km

Figure 2.

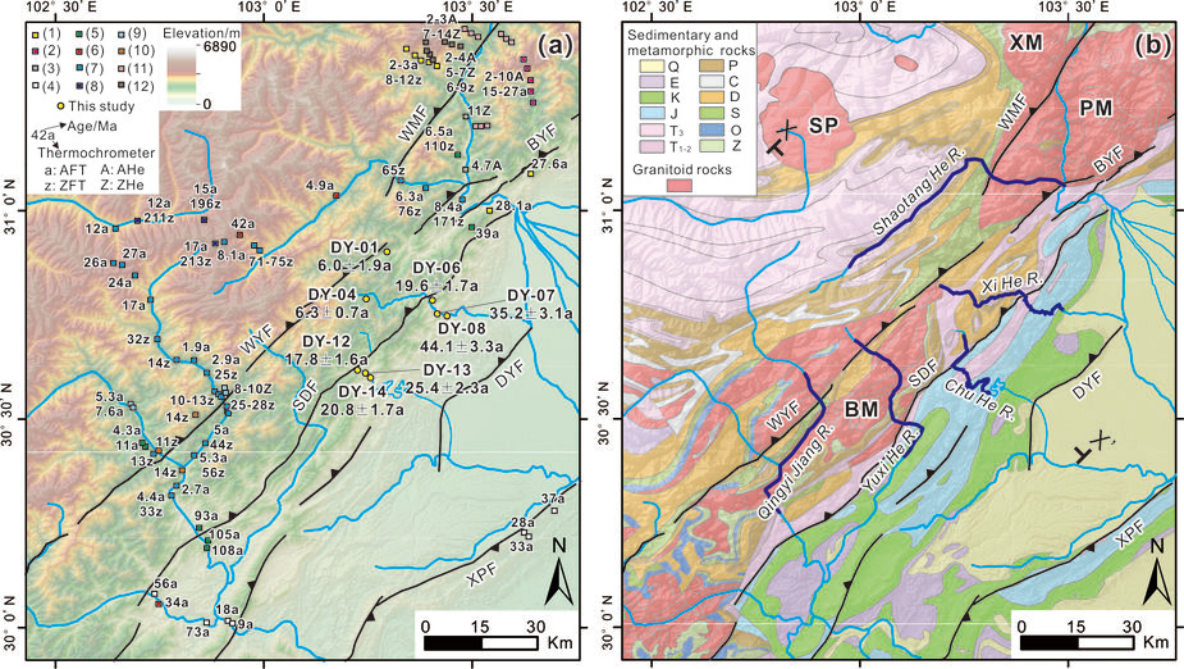
(a)
(b)
Elevation/m
6890
0
This study
Age/Ma
Thermochronometer
a: AFT A: AHe
z: ZFT Z: ZHe
DY-01 6.0±1.9a
DY-04 6.3±0.7a
DY-06 19.6±1.7a
DY-07 35.2±3.1a
DY-08 44.1±3.3a
DY-12 17.8±1.6a
DY-13 25.4±2.3a
DY-14 20.8±1.7a
WMF
BYF
SDF
DYF
XPF
Sedimentary and metamorphic rocks
Granitoid rocks
SP
XM
PM
BM
Shaotang He R.
Xi He R.
Chu He R.
Qingyi Jiang R.
Yuxi He R.
0 15 30 Km
N

Figure 3.

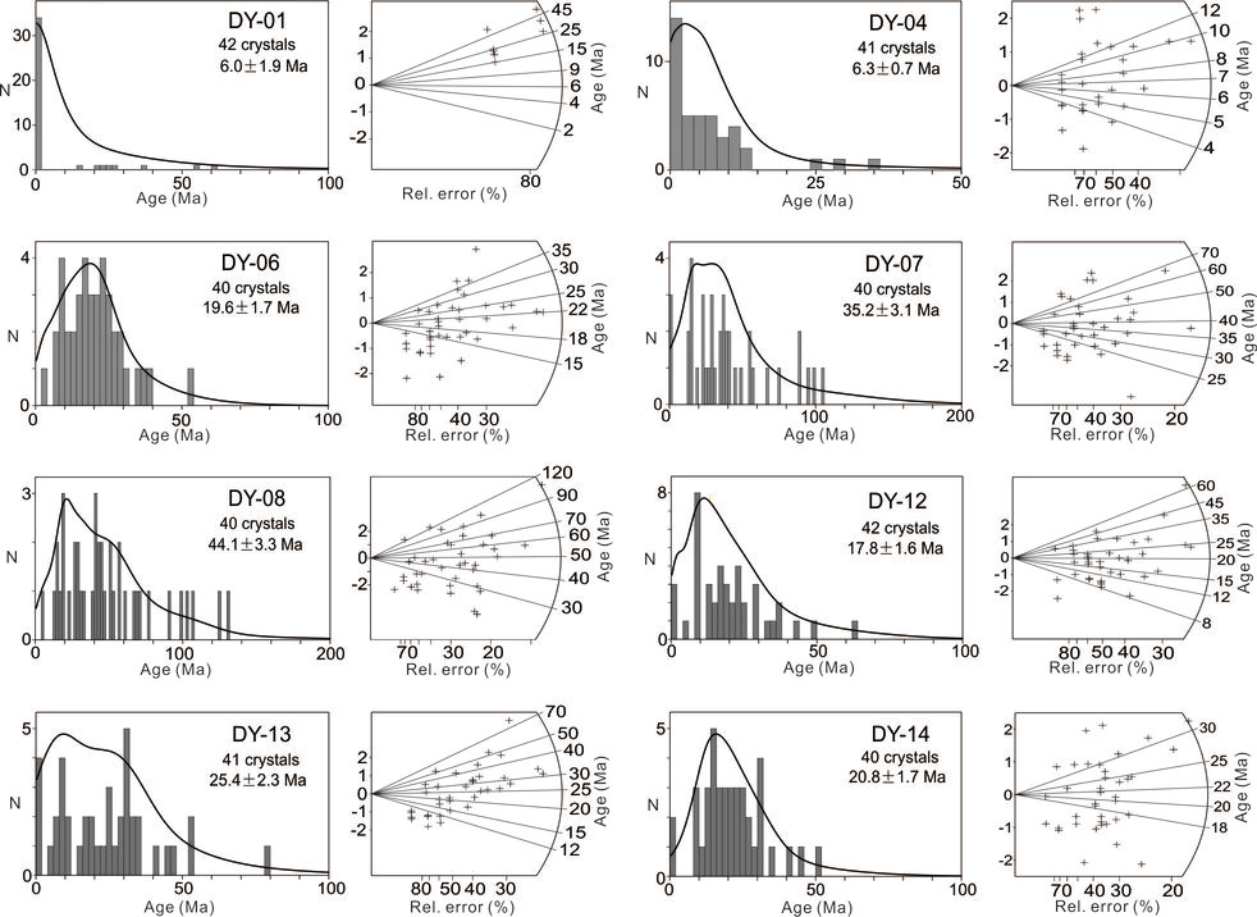
DY-01
42 crystals
6.0±1.9 Ma
DY-04
41 crystals
6.3±0.7 Ma
DY-06
40 crystals
19.6±1.7 Ma
DY-07
40 crystals
35.2±3.1 Ma
DY-08
40 crystals
44.1±3.3 Ma
DY-12
42 crystals
17.8±1.6 Ma
DY-13
41 crystals
25.4±2.3 Ma
DY-14
40 crystals
20.8±1.7 Ma
N
Age (Ma)
Rel. error (%)

Figure 4.

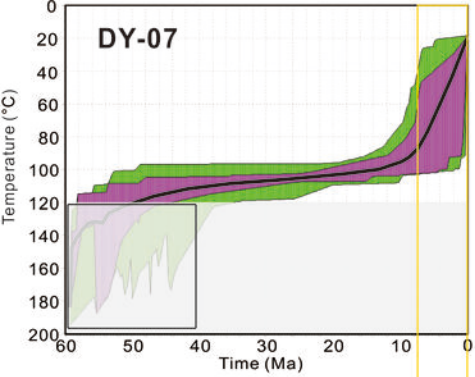
DY-07
Temperature (°C)
Time (Ma)

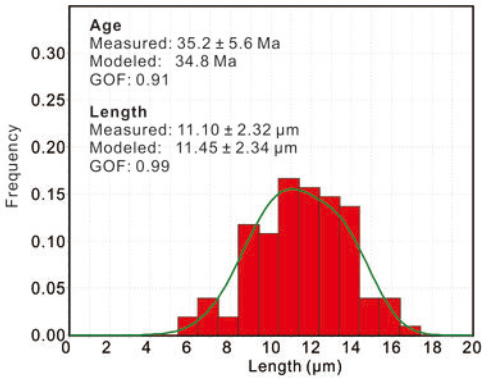
Age
Measured: 35.2 ± 5.6 Ma
Modeled: 34.8 Ma
GOF: 0.91
Length
Measured: 11.10 ± 2.32 μm
Modeled: 11.45 ± 2.34 μm
GOF: 0.99
Frequency
Length (μm)

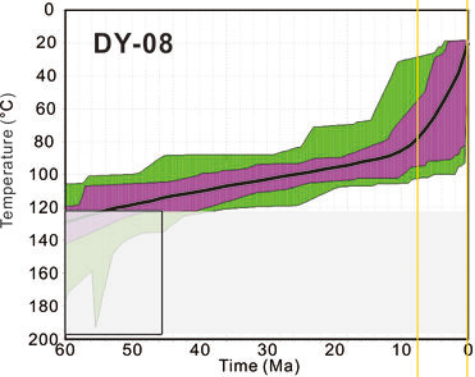
DY-08
Temperature (°C)
Time (Ma)

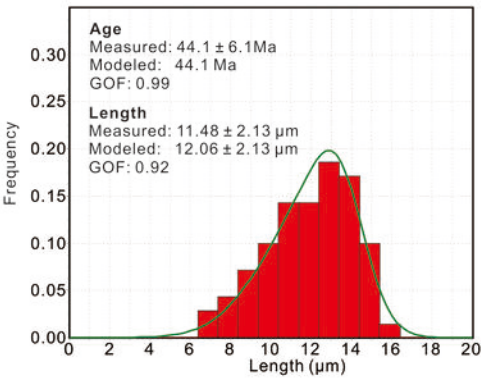
Age
Measured: 44.1 ± 6.1Ma
Modeled: 44.1 Ma
GOF: 0.99
Length
Measured: 11.48 ± 2.13 μm
Modeled: 12.06 ± 2.13 μm
GOF: 0.92
Frequency
Length (μm)

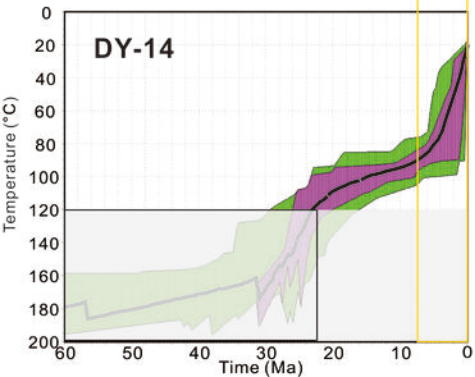
DY-14
Temperature (°C)
Time (Ma)

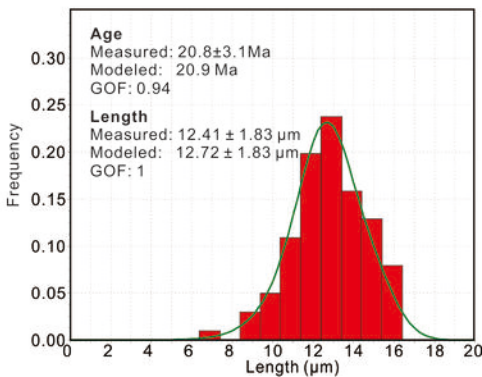
Age
Measured: 20.8±3.1Ma
Modeled: 20.9 Ma
GOF: 0.94
Length
Measured: 12.41 ± 1.83 μm
Modeled: 12.72 ± 1.83 μm
GOF: 1
Frequency
Length (μm)

Figure 5.

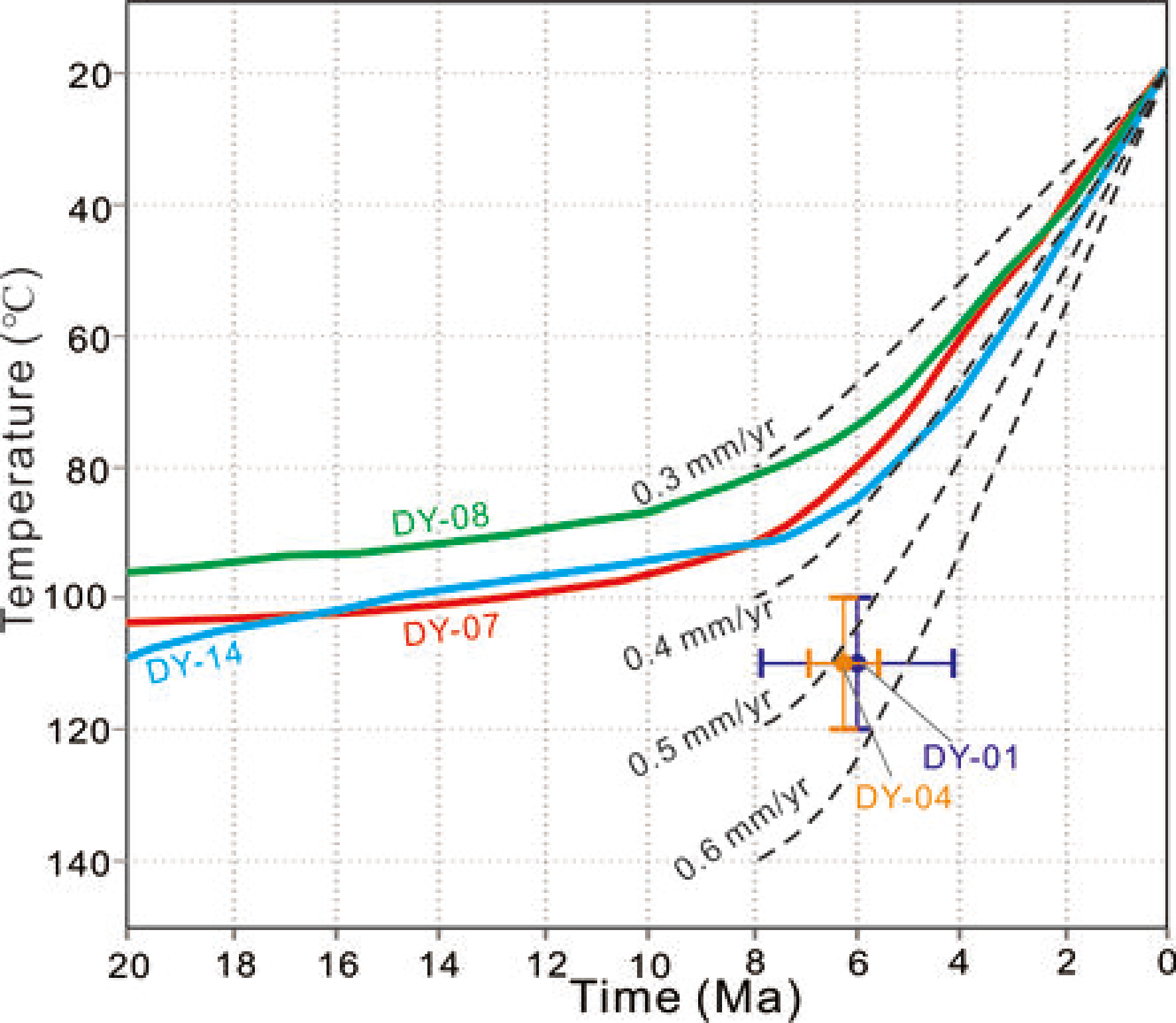
Temperature (°C)
20
40
60
80
100
120
140
20
18
16
14
12
10
8
6
4
2
0
Time (Ma)
DY-08
DY-07
DY-14
0.3 mm/yr
0.4 mm/yr
0.5 mm/yr
0.6 mm/yr
DY-01
DY-04

Figure 6.

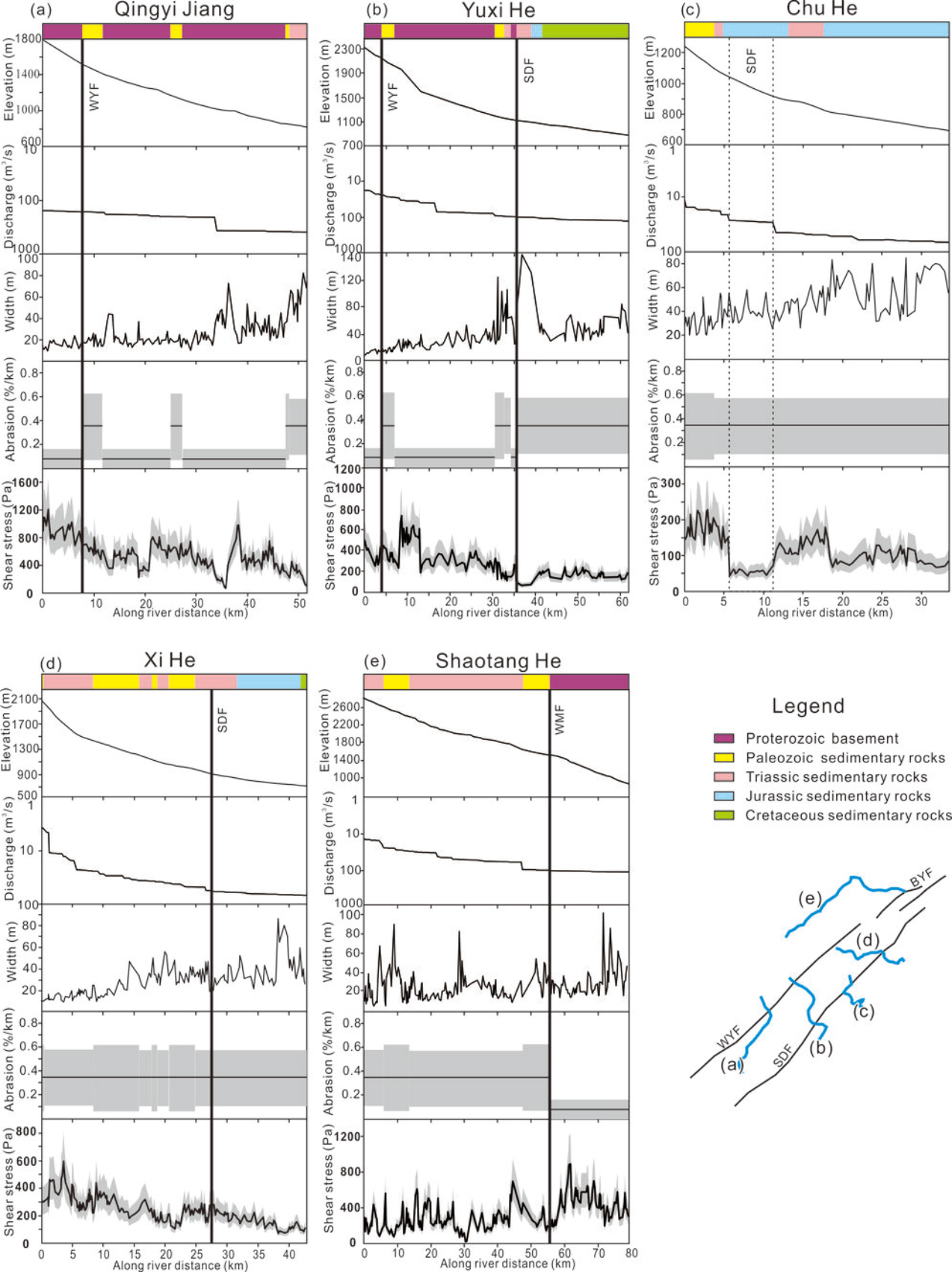
(a)
Qingyi Jiang
(b)
Yuxi He
(c)
Chu He
(d)
Xi He
(e)
Shaotang He
WYF
SDF
WMF
Elevation (m)
Discharge (m³/s)
Width (m)
Abrasion (%/km)
Shear stress (Pa)
Along river distance (km)
Legend
Proterozoic basement
Paleozoic sedimentary rocks
Triassic sedimentary rocks
Jurassic sedimentary rocks
Cretaceous sedimentary rocks
BYF

Figure 7.

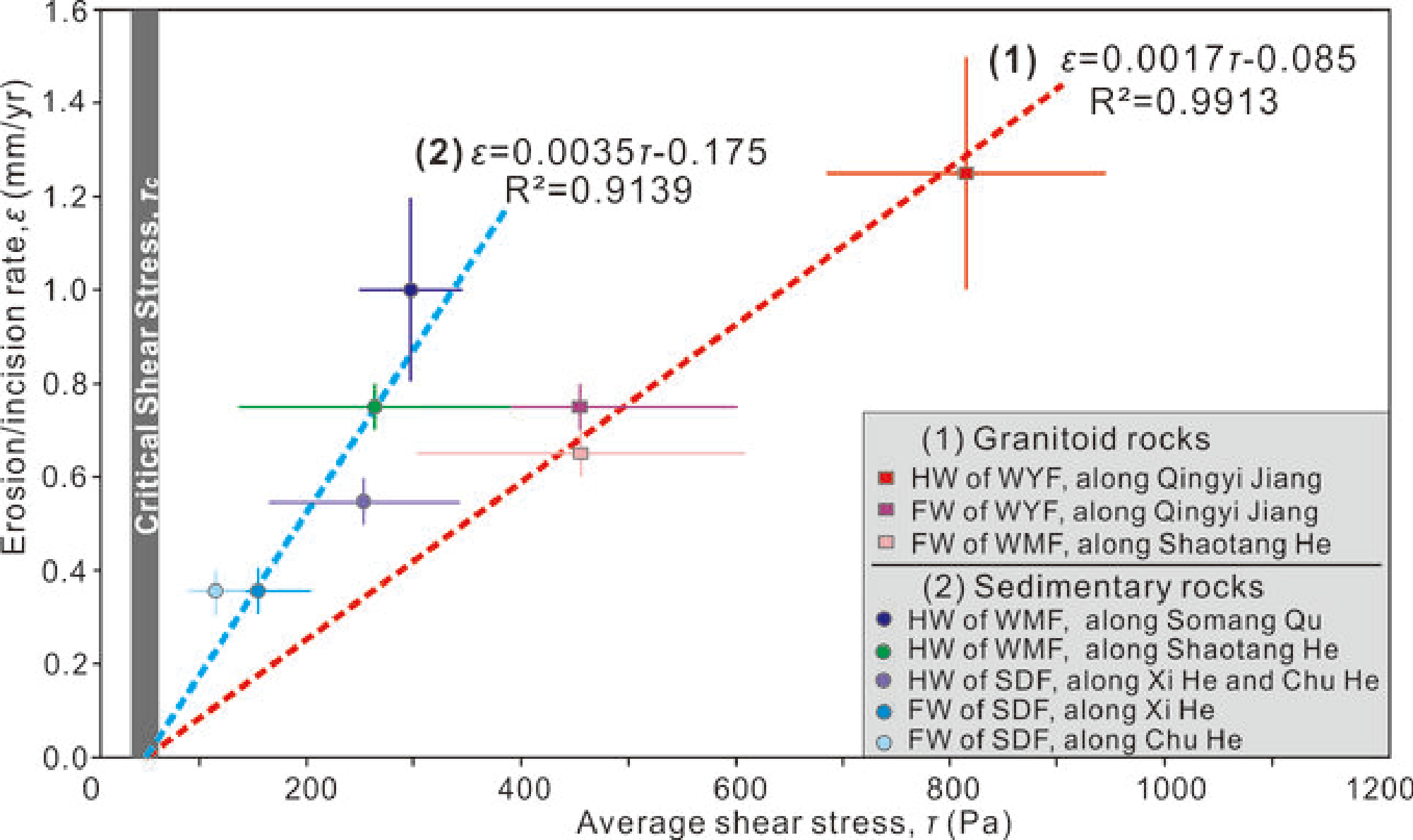
(1) ε=0.0017τ-0.085
R²=0.9913
(2) ε=0.0035τ-0.175
R²=0.9139
Critical Shear Stress, τc
Erosion/incision rate, ε (mm/yr)
Average shear stress, τ (Pa)
0.0
0.2
0.4
0.6
0.8
1.0
1.2
1.4
1.6
0
200
400
600
800
1000
1200
(1) Granitoid rocks
HW of WYF, along Qingyi Jiang
FW of WYF, along Qingyi Jiang
FW of WMF, along Shaotang He
(2) Sedimentary rocks
HW of WMF, along Somang Qu
HW of WMF, along Shaotang He
HW of SDF, along Xi He and Chu He
FW of SDF, along Xi He
FW of SDF, along Chu He

Figure 8.

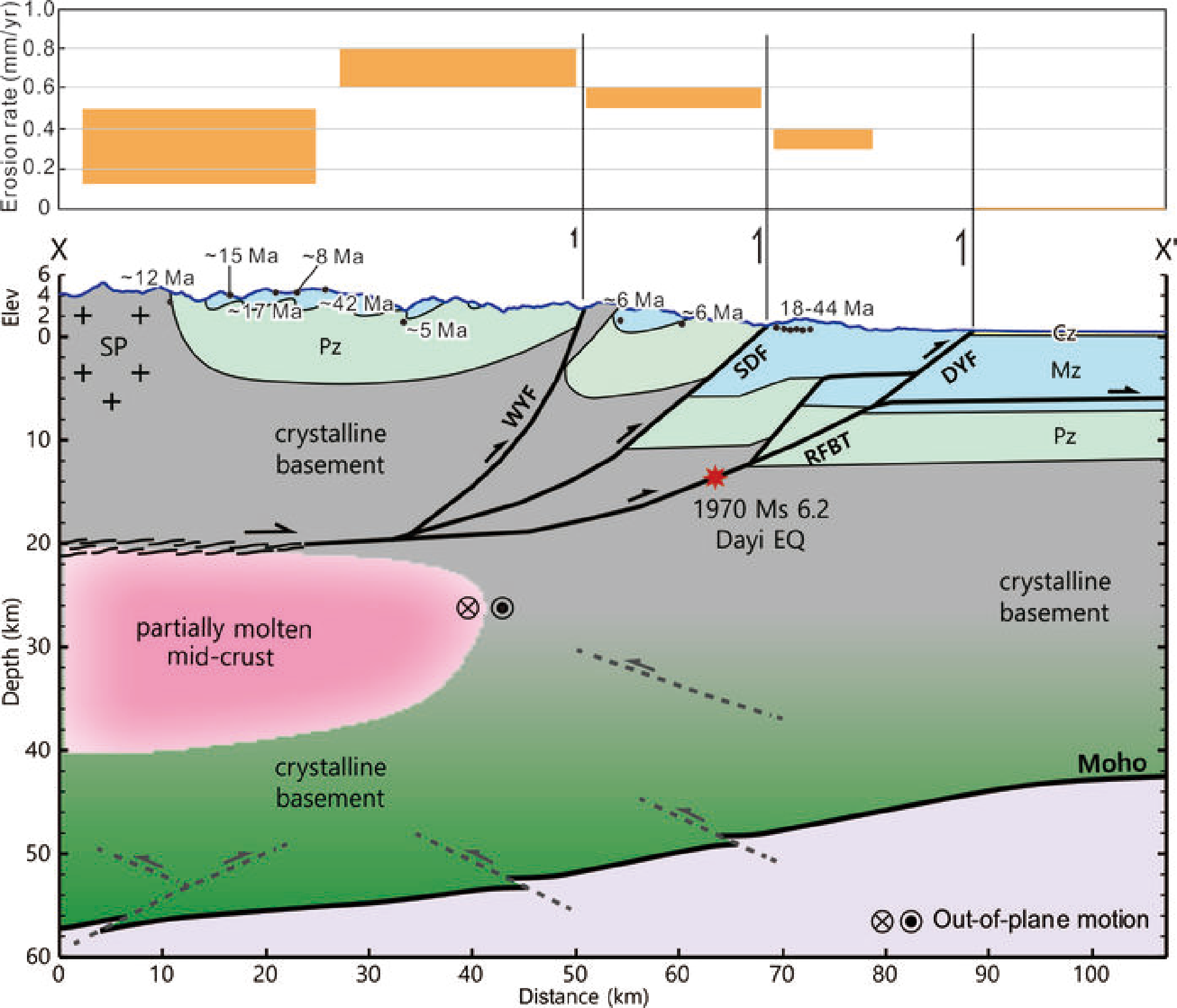
Erosion rate (mm/yr)
1.0
0.8
0.6
0.4
0.2
0
X
X'
1
1
1
Elev
6
4
2
0
~12 Ma
~15 Ma
~8 Ma
~17 Ma
~42 Ma
~5 Ma
~6 Ma
~6 Ma
18-44 Ma
SP
Pz
crystalline basement
WYF
SDF
DYF
RFBT
Cz
Mz
Pz
1970 Ms 6.2
Dayi EQ
partially molten mid-crust
crystalline basement
crystalline basement
Moho
Out-of-plane motion
Depth (km)
10
20
30
40
50
60
0
10
20
30
40
50
60
70
80
90
100
Distance (km)

Figure 9.

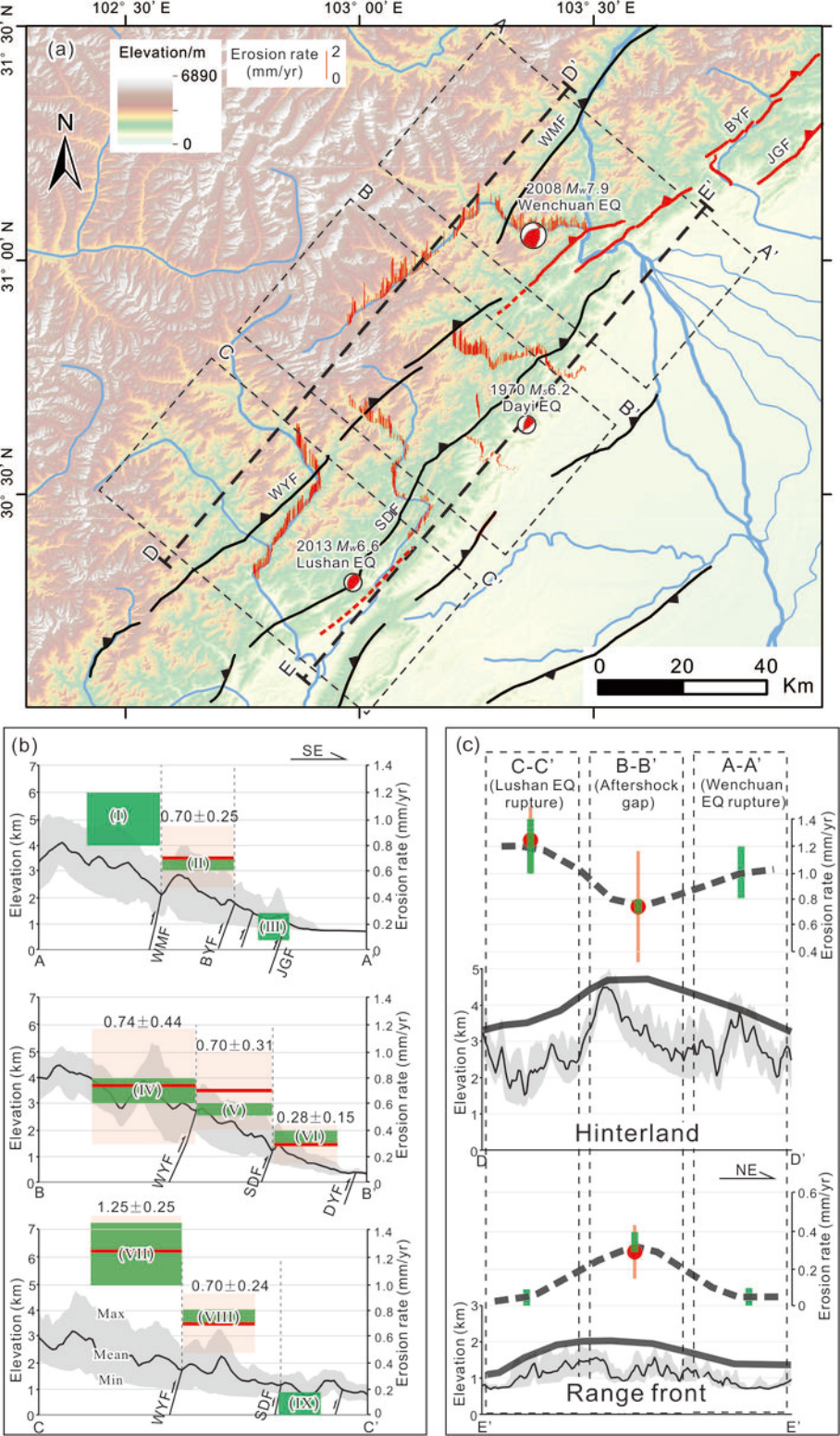
(a)
Elevation/m
6890
0
Erosion rate (mm/yr)
2
0
N
WMF
BYF
JGF
WYF
SDF
2008 Mw7.9 Wenchuan EQ
1970 Ms6.2 Dayi EQ
2013 Mw6.6 Lushan EQ
A
A'
B
B'
C
C'
D
D'
E
E'
0
20
40
Km
102° 30' E
103° 00' E
103° 30' E
31° 30' N
31° 00' N
30° 30' N
(b)
SE
Elevation (km)
Erosion rate (mm/yr)
(I)
0.70±0.25
(II)
(III)
WMF
BYF
JGF
A
A'
0.74±0.44
(IV)
0.70±0.31
(V)
0.28±0.15
(VI)
WYF
SDF
DYF
B
B'
1.25±0.25
(VII)
0.70±0.24
(VIII)
Max
Mean
Min
(IX)
C
C'
(c)
C-C'
(Lushan EQ rupture)
B-B'
(Aftershock gap)
A-A'
(Wenchuan EQ rupture)
Hinterland
D
D'
NE
Range front
E'
E'

Figure 10.

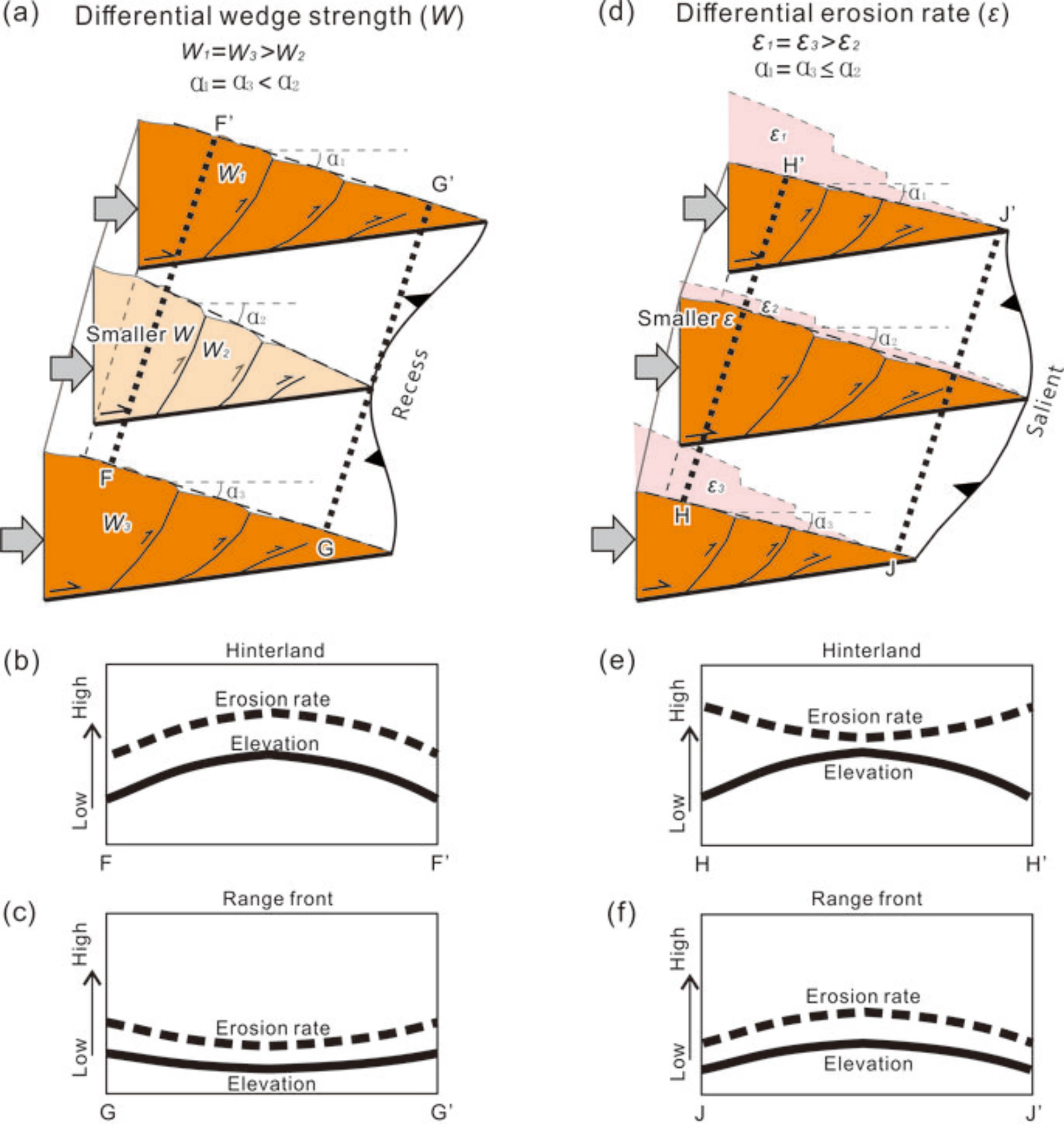
(a)
Differential wedge strength (W)
W1=W3>W2
α1=α3<α2
F'
W1
α1
G'
Smaller W
W2
α2
Recess
F
W3
α3
G
(d)
Differential erosion rate (ε)
ε1=ε3>ε2
α1=α3≤α2
ε1
H'
α1
J'
Smaller ε
ε2
α2
Salient
ε3
H
α3
J
(b)
Hinterland
High
Erosion rate
Elevation
Low
F
F'
(e)
Hinterland
High
Erosion rate
Elevation
Low
H
H'
(c)
Range front
High
Erosion rate
Low
Elevation
G
G'
(f)
Range front
High
Erosion rate
Low
Elevation
J
J'

Figure 11.

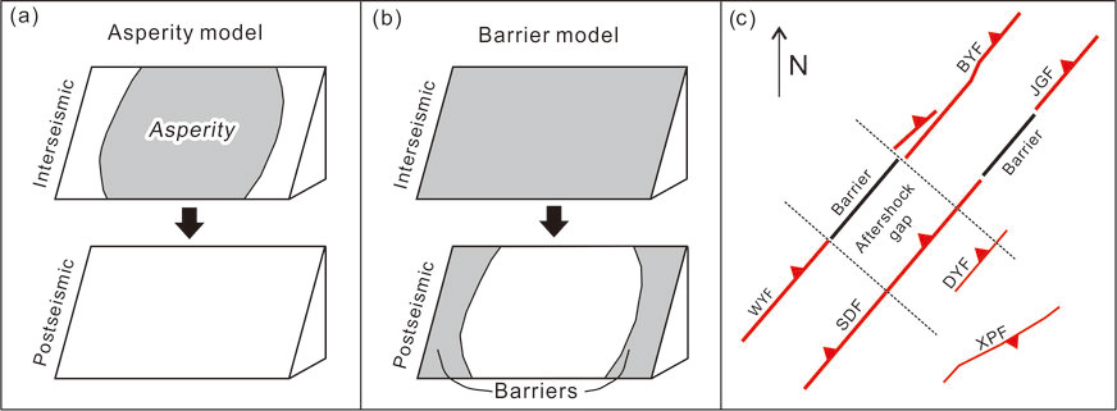
(a)
Asperity model
Interseismic
Asperity
Postseismic
(b)
Barrier model
Interseismic
Postseismic
Barriers
(c)
N
BYF
JGF
Barrier
Barrier
Aftershock gap
WYF
SDF
DYF
XPF

Table 1 AFT data at the aftershock gap of the Longmen Shan.

Sample	Latitude (°N)	Longitude (°E)	Elevation (m)	Lithology	Crystal	RhoS	Ns	RhoI	Ni	RhoD	Nd	P (%)	Age (Ma)
DY-1	30.8956	103.2975	1274	Granitoid	42	0.12	11	6.053	556	17.28	4798	21.76	6.0±1.9
DY-4	30.7825	103.2283	1580	Sandstone	41	0.466	99	22.472	4776	17.28	4798	17.3	6.3±0.7
DY-6	30.7844	103.4031	813	Sandstone	40	1.536	281	20.831	3812	15.25	4798	18.88	19.6±1.7
DY-7	30.7522	103.4222	763	Sandstone	40	1.741	280	14.912	2398	17.28	4798	0.27	35.2±3.1
DY-8	30.7503	103.2183	684	Sandstone	40	3.03	641	18.248	3860	15.25	4798	0	44.1±3.3
DY-12	30.6222	103.2183	919	Sandstone	42	1.037	226	17.513	3818	17.28	4798	0.01	17.8±1.6
DY-13	30.6125	103.23722	849	Sandstone	41	1.685	234	17.662	2453	15.25	4798	0.83	25.4±2.3
DY-14	30.6036	103.25528	845	Sandstone	40	1.827	355	26.493	5149	17.28	4798	14.77	20.8±1.7